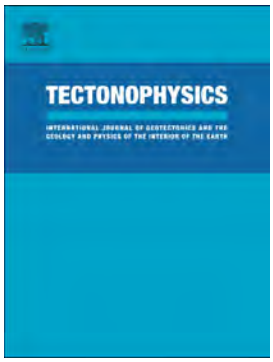

Strain indicators and magnetic fabric in intraplate fault zones: Case study of Daroca thrust, Iberian Chain, Spain

A.M. Casas-Sainz, A. Gil-Imaz, J.L. Simón, E. Izquierdo-Llavall, L. Aldega, T. Román-Berdiel, M.C. Osácar, Ó. Pueyo-Anchuela, M. Ansón, C. García-Lasanta, S. Corrado, C. Invernizzi, C. Caricchi

PII: S0040-1951(18)30079-9
DOI: doi:10.1016/j.tecto.2018.02.013
Reference: TECTO 127785

To appear in: *Tectonophysics*

Received date: 13 July 2017
Revised date: 15 February 2018
Accepted date: 16 February 2018

Please cite this article as: A.M. Casas-Sainz, A. Gil-Imaz, J.L. Simón, E. Izquierdo-Llavall, L. Aldega, T. Román-Berdiel, M.C. Osácar, Ó. Pueyo-Anchuela, M. Ansón, C. García-Lasanta, S. Corrado, C. Invernizzi, C. Caricchi , Strain indicators and magnetic fabric in intraplate fault zones: Case study of Daroca thrust, Iberian Chain, Spain. The address for the corresponding author was captured as affiliation for all authors. Please check if appropriate. Tecto(2017), doi:10.1016/j.tecto.2018.02.013

Strain indicators and magnetic fabric in intraplate fault zones: case study of Daroca thrust, Iberian Chain, Spain

A.M. Casas-Sainz[1], A. Gil-Imaz[1], J.L. Simón[1], E. Izquierdo-Llavall[2,3], L. Aldega[4], T. Román-Berdiel[1*], M.C. Osácar[1], Ó. Pueyo-Anchuela[1], M. Ansón[1], C. García-Lasanta[1], S. Corrado[5], C. Invernizzi[6] & C. Caricchi[7]

[1]*Departamento de Ciencias de la Tierra, Instituto de Investigación en Ciencias Ambientales (IUCA), Universidad de Zaragoza, Pedro Cerbuna 12, 50009 Zaragoza, Spain*

[2]*Departament de Geodinàmica i Geofísica, Universitat de Barcelona, Martí i Franquès s/n, 08028 Barcelona, Spain*

[3]*Laboratoire des Fluides Complexes et leurs Réservoirs, CNRS (UMR 5150), Université de Pau, France*

[4]*Dipartimento di Scienze della Terra, Sapienza Università di Roma, Italy*

[5]*Dipartimento di Scienze, Università Roma TRE, Largo San Leonardo Murialdo 1, 00146 Roma, Italy*

[6]*Scuola di Scienze e Tecnologie, sezione Geologia, Università di Camerino, Italy*

[7]*Instituto Nazionale di Geofisica e Vulcanologia, Via di Vigna Murata 605, 00143 Roma, Italy*

**Corresponding author (e-mail: mtdjrb@unizar.es)*

Abbreviated title: **AMS in intraplate shallow fault zones**

Abstract: Anisotropy of magnetic susceptibility (AMS) has been applied to the study of shallow fault zones, although interpretation of the results requires establishing clear relationships between petrofabric and magnetic features, magnetic behavior of fault rocks, and an extensive knowledge of P-T conditions. In this work, we demonstrate that magnetic methods can be applied to the study of heterogeneous fault zones, provided that a series of requisites are met. A major fault zone within the Iberian plate (Daroca thrust), showing transpressional movements during Cenozoic time was chosen for this purpose, because of the exceptional outcrops of fault gouge and microbreccia and its relevance within the context of the northeastern Iberian Plate. Magnetic fabrics were analysed and the results were compared with foliation and S-C structures measured within the fault zone. Clay mineral assemblages suggest maximum burial depths shallower than 2 km (<60-70°C) for fault rocks in the footwall of the Daroca thrust. The orientation of the AMS axes is consistent with mesostructural strain indicators: k_{min} parallels the mean pole to S, or it is intermediate between S and C poles; k_{max} is oriented at a high angle (nearly orthogonal in overall) to the transport direction, which can be explained from both deformational and mineralogical controls. Both magnetic fabrics and kinematic indicators are consistent with a reverse movement for most of the fault zone.

Keywords: Anisotropy of magnetic susceptibility, fault rock, transport direction, transpression, kinematic indicator.

1. Introduction

Defining the kinematics of major fault zones in intraplate areas is a significant issue because of its implications on the movement of crustal blocks and the formation of intra-plate mountain belts (e. g. Ziegler, 1989; Dyksterhuis, 2008; Kley and Voight, 2008). These zones of weakness are commonly long-lived structures involving the basement, and are linked to rifting and subsequent inversion processes (Gabrielsen *et al.*, 1999; Scheck *et al.*, 2002; Elías-Herrera and Ortega-Gutiérrez, 2002; Otto, 2003; Scheck-Wenderoth and Lamarche, 2005; De Vicente *et al.*, 2009, 2011).

In addition, because of the structural complexity of fault zones in intraplate areas (and of their kinematic indicators) at shallow crustal levels, a combination of techniques is a convenient approach for deciphering their kinematics. In this sense, anisotropy of magnetic susceptibility (AMS) has demonstrated to be a reliable method for unravelling the kinematic evolution of faults (Solum and van der Pluijm, 2009; Levi *et al.,* 2014; Moreno *et al.*, 2014; Pomella, 2014; Braun *et al.,* 2015; Keskinva *et al.*, 2016; Casas *et al.*, 2017) due to the possibility of averaging datasets even where structures are not well developed at the outcrop scale.

Nevertheless, some drawbacks to this approach do exist, since the relationship between magnetic fabrics and petrofabric of fault zones at shallow crustal levels can be ambiguous because of:

1) The heterogeneity of the petrofabric itself, especially when cataclasis is the main deformation mechanism and foliations and/or lineations are discontinuous or interrupted along the fault zone (Billi and Storti, 2004). Combination of different mechanisms (semi-brittle to brittle) can result in different microstructures that, although kinematically consistent, overprint or modify the original fabric (Ben-Zion and Sammis, 2003; Faulkner *et al.*, 2003). Moreover, movements along distinct transport directions during the evolution of fault zones strongly contribute to increase such heterogeneity.

2) Neoformation of different mineral phases (both para- and ferromagnetic) coeval to fault activity, and favoured by thermal/mechanical processes (Chou *et al.,* 2012a; 2012b; 2014). Sequential crystallization can result in the development of different subfabrics, which may or not coincide to each other depending on the particular kinematics of faults and the response of fault rocks to shear. Controls on the conditions of development of magnetic fabrics are therefore of major importance and can also give clues about the origin of these fabrics or remagnetization processes responsible for the change of magnetic properties of rocks. In this sense, understanding the kinematics of fault zones also involves knowing the thermal conditions and mechanical behaviour of fault rocks associated with thrusting, together with the depth of thrusting and the rocks provenance. Palaeothermal indicators from clay minerals have been proven useful for studying fault rocks and provide information on fluid circulation, water/rock ratio, frictional heating and depth of deformation (Vrolijk and Van der Pluijm, 1999; Schleicher *et al.,* 2012; Balsamo *et al.*, 2014, Smeraglia *et al.*, 2016).

In this paper we explore the applicability of AMS and palaeothermal indicators from clay minerals to study fault gouge and microbreccia, up to several tens of metres thick, along an intra-plate fault zone (Daroca thrust, Aragonian Branch of the Iberian Chain). We intend to define the depth at which deformation occurred and to unravel its large-scale kinematics. The interest for this study is two-fold: i) from a methodological point of view, this is a significant contribution to establish relationships between magnetic properties and tectonic processes in fault rocks formed at shallow depths within the crust, which can be of interest in view of the possibility of wholesale application of magnetic techniques to other areas; ii) from the regional point of view, the definition of the tectonic regime during the Cenozoic in a representative area of the Iberian Chain can shed light on the evolution of the Iberian plate and the different mechanisms involved in fault re-activation and intra-plate deformation. Techniques used include structural analysis, X-ray diffraction, and a variety of magnetic methods, namely room-temperature and low-temperature AMS, thermomagnetic (k *vs* T) curves, and thermal and AF demagnetization of NRM to investigate the magnetic mineralogy.

2. Geological Setting

The Iberian Range (Fig. 1A) is an intraplate mountain chain resulting from deformation during the Cenozoic, driven by convergence between Europe, Africa and Iberia (Alvaro *et al.*, 1979; Casas and Faccenna, 2001; Capote *et al.*, 2002; De Vicente, 2004; De Vicente *et al.*, 2009). Conversely to other intra-plate uplifts in Iberia that mainly involve the Palaeozoic basement (De Vicente *et al.*, 2007; Fernández-Lozano *et al.*, 2011), the Iberian Chain resulted from inversion of Mesozoic sedimentary basins (De Vicente, 2004), except for its central zone (Aragonian Branch) where a thick Palaeozoic sequence (up to 11 km, Cortés-Gracia and Casas-Sainz, 1996; Calvín-Ballester and Casas, 2014) was re-folded during the Cenozoic compression with a NW-SE trend. In this sector, two large, Palaeozoic-cored structural highs (amplitude 2 km, wavelength 25 km in average, Casas-Sainz and Cortés-Gracia, 2002), separated by the Cenozoic Calatayud basin, define the structure of the chain (Fig. 1B). Crustal-scale strike-slip faults, probably inherited from the Late-Variscan fracturing episodes (Arthaud and Matte, 1975, 1977) can be recognized within the Aragonian Branch (De Vicente *et al.*, 2011; Gutiérrez *et al.*, 2012; Casas *et al.*, 2017). They are roughly parallel to the Cenozoic structural trend (NW-SE) and cut across the Palaeogene and Neogene infill of intra-mountain sedimentary basins. One of these major faults is the Daroca thrust, which constitutes the southern boundary of the Calatayud basin (Colomer and Santanach, 1988).

3. Structure

The Daroca thrust involves the Palaeozoic series (Lower Cambrian) typical of this sector of the Iberian Chain in its hanging-wall block, and the Miocene sequence of the Calatayud basin in its footwall block. The Cambrian sequence consists of dolostones and marls (Ribota Fm.), sandstones and mudstones (Huérmeda, Daroca, Valdemiedes and Murero Fms.; Carls, 1991). The syntectonic Middle Miocene series mainly consists of clastic sediments (conglomerates, sandstones and shales), deposited in alluvial fans sourced in the uplifted Aragonian Branch, which grade to limestones and gypsum towards the basin center (Villena *et al.*, 1991). The uppermost units infilling the Calatayud basin are Upper Miocene to Lower Pliocene in age. Finally, Upper Pliocene-Pleistocene conglomerates fill the Daroca Plio-Quaternary half-graben, subsequently developed in the southern block of the Daroca fault owing to its negative inversion during recent extensional deformation (Colomer, 1987; Gracia, 1992; Gutiérrez *et al.*, 2008).

The Daroca thrust is an outstanding feature within the Aragonian Branch of the Iberian Chain, making a part of a NW-SE alignment of faults involving the Palaeozoic, the Mesozoic cover and the Cenozoic syn-tectonic deposits (Guimerà and Alvaro, 1990; Alvaro, 1991). The intense fracturing in the surroundings of this thrust strongly contrasts with the monotonous southwards dip (45° to 55°S) of the rather undisturbed, 10-km-thick Palaeozoic sequence (Cambrian to Ordovician, Alvaro and Zamora, 2011) in its southern block (Fig. 2).

The Daroca thrust extends along 40 km with an overall NW-SE direction parallel to the main trend of the Iberian Chain (Fig. 1B). It constitutes the southern margin of the Calatayud basin, essentially filled with Miocene deposits. At several sites along its trace, Palaeozoic rocks appear in mechanical contact with red clastic Middle Miocene deposits, while in other areas younger units (Middle-Upper Miocene in age) lap onto the thrust front. The occurrence of several *en-échelon* arranged segments have been related to a strike-slip, right-lateral component within the overall structure (Julivert, 1954; Colomer, 1987; Colomer and Santanach, 1988).

In the surroundings of Daroca town, particularly good exposures show the main thrust surface making the boundary between Middle Miocene sediments (footwall) and Cambrian dolostones (hanging-wall) (Fig. 2A). Here, the thrust shows two clearly defined segments: (i) a main footwall ramp dipping 30° to 40°S, and (ii) a frontal footwall flat where the thrust surface dips shallowly (5-10°) towards the north; such dip is probably due to gentle folding after thrust emplacement (Figs. 2B, 2C). At the thrust front, the overturned limb of a recumbent fold defined by Cambrian dolostones lie onto the footwall flat of Middle Miocene conglomerates (Fig. 2D). The irregular morphology of the thrust front, the ramp-flat change within the homogeneous Miocene detrital sequence, and the presence of small extensional faults confined to the hanging-wall block are compatible with an epiglyptic origin (Mattauer, 1973).

Well-developed microbreccia and fault gouge, with a total thickness between 0.25 and 40 m and including blocks composed of Palaeozoic rocks, crop out in the fault zone (Ansón *et al*., 2017). The thickest fault-rock band is linked to the thrust ramp, and its most conspicuous exposure is located south of Daroca, at the exit of a tunnel (*La Mina*) excavated in the XVIth century as a diversion channel for flood control (Figs. 2E, 2F). At this site, the main thrust plane is oriented 130, 15 S (strike, dip, sense of dip). Broad banding determined by a succession of microbreccia, fault gouge and large fragments of Cambrian dolostones, as well as penetrative south-dipping cleavage, can be observed within the fault rocks (Ansón *et al*., 2017). A thin veneer of fault rocks also

appears at the frontal sector of the Daroca thrust, close to the contact between Palaeozoic dolostones and Miocene detrital deposits and affecting both lithological domains.

The Daroca thrust is cut by a WNW-ESE striking, south dipping extensional fault that makes the contact between the Palaeozoic block and the Plio-Pleistocene infill of the Jiloca half-graben (Figs. 2A, 2B). This high-angle normal fault is exposed at *La Mina* site, where Miocene red clastic deposits occupy its hanging-wall block, overlain by Upper Pliocene conglomerates (Figs. 2E, 2F). Such Miocene deposits probably represent those that formerly lapped onto the thrust front (therefore located at a higher position), and were subsequently downthrown (a few hundreds of meters) into the Jiloca half-graben.

4. Methods

This work includes a total of 16 measuring sites located along the Daroca fault zone (Fig. 2A), 12 of which are focused on structural analysis, 4 were sampled for X-ray diffraction and 6 for magnetic analysis (Tables 1, 2 and 3). Fault rocks were analysed along two main sectors within the fault zone located close to the Daroca town, where fault rocks show good exposures, and samples from the different levels forming the fault damage zone could be collected. The southern sector is associated with a thick fault gouge (sites 1 to 5, 8 to 10 from the base to the top of the fault damage zone), while the northern sector is related to a thinner fault breccia (sites 11 and 12) and microbreccia (sites 13 to 16). Additionally, two sites were surveyed in Cenozoic units of the footwall (sites 6 and 7) of the southernmost fault zone. In all these sites, the geometry and orientation of structures at the meso- and micro-scale were determined from direct outcrop observations and measurements, as well as from polished and thin sections of oriented samples.

4.1. Structural analysis

A detailed structural analysis from the Daroca fault zone at meso and micro-scale was performed. The outcrop of fault rocks allows for a continuous sampling at different distances from the main fault surface to be done, especially in the hanging-wall block. Measurements of foliations and S-C-like structures in 12 sites along the fault trace were carried out (Table 1). Most of them correspond to the fault gouge and brecciated Cambrian dolostones and marls of the hanging-wall; the remaining, more scattered data, come from Miocene clastics of the footwall block.

In order to establish the relationship between fault-related deformation and rock composition, a number of detailed litho-structural transects across the Daroca fault zone have been carried out (Figs. 3 and 4). A litho-structural classification of different units along those transects has been achieved using three parameters: 1) predominant lithology, 2) rock texture, and 3) tectonic structures.

Directional analysis was performed, for each site and for the whole study area, on equal-area stereoplots using the Stereonet software (Allmendinger *et al.*, 2013; Cardozo and Allmendinger, 2013). In most cases, transport directions were inferred from S-C structures (line belonging to both the mean C plane and the movement plane, therefore orthogonal to the S/C intersection line). Locally, displacement vectors were inferred from direct measurement of fault striations.

Microtectonic analysis including fabric characterization and interpretation of deformation mechanisms was carried out from 5 thin sections of microbreccia samples analysed under a polarizing microscope (Table 1).

4.2. X-ray diffraction of fault rocks

X-ray diffraction analyses were carried out with a Scintag X1 X-ray system (CuKα radiation) at 40 kV and 45 mA. Randomly-oriented whole-rock powders were run in the 2-70 °2θ interval with a step size of 0.05 °2θ and a counting time of 3 s per step in order to determine the whole-rock composition of fault rocks. Oriented air-dried and ethylene-glycol solvated samples of the <2 μm (equivalent spherical diameter) grain-size fraction were scanned from 1 to 48 °2θ and from 1 to 30 °2θ respectively with a step size of 0.05 °2θ and a count time of 4 s per step. Either detrital and neoformed minerals in the <2 μm grain-size fraction were investigated in order to determine the maximum burial conditions the fault rocks underwent during thrusting. In particular, mixed layers illite-smectite (I–S) can be used as indicators of the thermal evolution of sedimentary successions (Aldega *et al.*, 2007; 2014; Corrado *et al.*, 2010; Izquierdo-Llavall *et al.*, 2013), for evaluating the amount of denudation of the sedimentary and/or tectonic overburden, removed by erosion and/or tectonics (Aldega *et al.*, 2011; 2017; Di Paolo *et al.,* 2012, Caricchi *et al.*, 2015; Schito *et al.*, 2017) and determining the depth at which deformation occurred in fold-and-thrust belts (Meneghini *et al.,* 2012, Carlini *et al.*, 2013, Carminati *et al.*, 2013, 2016).

The illite content in mixed layers I-S was determined, according to Moore and Reynolds (1997), using the delta two-theta method after decomposing the composite peaks between 9-10 °2θ and 16-17 °2θ. The I-S ordering type (Reichweite parameter, R; Jagodzinski, 1949) was determined by the position of the I001-S001 reflection between 5 and 8.5 °2θ (Moore and Reynolds 1997). Peaks in relative close position were selected for clay mineral quantitative analysis of the <2 μm grain-size fraction in order to minimize the angle-dependent intensity effect. Composite peaks were decomposed using Pearson VII functions and the WINXRD Scintag associated program. Integrated peak areas were transformed into mineral concentration by using mineral intensity factors as a calibration constant (for a review, see Moore and Reynolds 1997).

4.3. Magnetic techniques

Sampling to apply magnetic techniques was carried out in 6 sites across the fault gouge and microbreccia (Table 1) using an electrical, water-cooled drill. Sites consist of 8 to 16 in situ drilled cores, so that a total of 67 cylindrical standard specimens (2.5 cm in diameter, 2.1 cm in height) were obtained. In addition, 122 cubic standard specimens (2.1 x 2.1 cm) were cut from two hand blocks extracted from two of the sites (2 and 9) and considered for AMS analysis.

AMS measurements were done with a KLY-3S susceptibility meter (AGICO, Czech Republic) in the Magnetic Fabrics Laboratory of the University of Zaragoza. For each specimen, the bulk susceptibility and the orientation of the maximum (k_{max}), intermediate (k_{int}) and minimum (k_{min}) axes of the magnetic ellipsoid were obtained. The shape of this ellipsoid and the degree of magnetic fabric development were defined by two parameters: (1) the corrected degree of anisotropy, P', that provides a first indication of rock deformation and preferred mineral orientation, and (2) the shape parameter, T, varying between 0≥T≥-1 (prolate ellipsoids) and 0≤T≤1 (oblate ellipsoids). P' and T parameters are defined as (Jelinek, 1981):

$$P' = \exp\sqrt{2\left[\left(\eta_1 - \eta_m\right)^2 + \left(\eta_2 - \eta_m\right)^2 + \left(\eta_3 - \eta_m\right)^2\right]},$$

$$T = \frac{2\eta_2 - \eta_1 - \eta_3}{\eta_1 - \eta_3}$$

where μ1, μ2 and μ3 represent ln(k_{max}), ln(k_{int}) and ln(k_{min}), respectively, and μm = (μ1 + μ2 + μ3)/3. Mean site values were computed using Jelinek statistics (Jelinek, 1978) by means of the Anisoft 4.2 program (Chadima and Jelinek, 2009).

To define mineral carriers of magnetic susceptibility, thermomagnetic susceptibility curves (k-T curves) were performed in 6 selected samples, one per site (Table 1). The shape of these curves (ranging between 40 and 700°C) provides a first approximation to the magnetic behaviour and mineralogy of magnetic susceptibility carriers: hyperbolic susceptibility decay at the initial part of the curves points to the presence of paramagnetic minerals whereas sharp susceptibility decays are related to ferromagnetic phases. The specific ferromagnetic minerals can be identified through their Curie or Néel temperatures that define the transition from ferromagnetic *s.l.* to paramagnetic behaviours. Curves were obtained on powdered samples (45-55 mg) using a KLY-3S Kappabrigde combined with a CS-3 furnace (AGICO Inc., Czech Republic). Heating rates were of 12-13°C/min and measurements were performed in Ar atmosphere to avoid mineral oxidation during heating. Raw data were corrected for the empty furnace and processed using Cureval 8.0 (Chadima and Hrouda, 2009).

To better characterize the ferromagnetic minerals present in the microbreccia, a total of 36 specimens were subjected to thermal (and occasionally AF) demagnetization of the NRM using an AC furnace (model TD48) at the Palaeomagnetism Laboratory of the University of Burgos. Magnetization was measured with a 2-G cryogenic magnetometer and susceptibility was monitored during thermal demagnetization using a Bartington MS2 dual frequency susceptibility meter. Temperature steps ranged between 10 and 50°C, up to a maximun of 680°C, based on the behaviour of pilot samples.

Magnetic fabric results were complemented with low temperature AMS measurements (LT-AMS). These experiments enhance the magnetic susceptibility of paramagnetic minerals as determined by the Curie-Weiss law (k = C/(T-Tc)) where k is the paramagnetic susceptibility, C is the Curie constant, T is the absolute temperature and Tc is the Curie temperature (Ritcher and Van der Plujim, 1994; Dunlop and Özdemir, 1997; Parés and Van der Pluijm, 2002). Assuming purely paramagnetic phases with a paramagnetic Curie temperature around 0 K, the expected magnetic susceptibility at low temperature (77K) is approximately 3.8 times higher than at room temperature (as the ratio of temperatures: 292/77, Hirt and Gehring, 1991; Ritcher and Van der Pluijm, 1994; Lüneburg *et al.,* 1999). Low temperature magnetic fabrics were measured on 12

standard specimens (from sites 8 and 16) using the KLY-3S Kappabridge susceptometer. Sites were selected depending on their location (site 8 in the southern sector and site 16 in the northern sector), and depending on the orientation and shape of their magnetic ellipsoid at room temperature (oblate in site 8 and prolate in site 16). Samples were first submerged in liquid nitrogen (-195°C/77K) for 30-40 minutes before measurements and cooled down again for 10 minutes between each of the three spinner positions required by the KLY-3S Kappabrigde (as in Oliva-Urcia *et al.,* 2010).

5. Results

5.1. Meso- and microstructural deformation: kinematic analysis

Deformation structures within the fault gouge and microbreccia at meso- and micro-scale indicate a brittle-ductile behavior during deformation. They are distributed across a shear zone a few centimeters to several meters thick, mainly in the gouge and breccia resulting from the hanging-wall block deformation at the main ramp, although also Middle Miocene clastic rocks of the footwall block underwent internal shear deformation expressed as small-scale structures.

A pervasive S foliation oblique to the thrust plane occurs in every outcrop, becoming more penetrative as approaching the thrust surface (Figs. 3B, 3C). S-C-like structures develop within lutite and microbreccia horizons (Figs. 3B, 3C). The angle between S and C planes shows a wide range, usually between 17° and 40°, revealing strong heterogeneity of shear strain. No consistent relationship has been noticed between that angle and factors such as composition or thickness of the shear band. Some of the surveyed outcrops show imbricated sigmoidal horses evincing the contribution of brittle deformation to the total shear (Figs. 3A, 3B, 3C).

The most intensively surveyed sector includes the thick fault rock band associated with the thrust ramp South of Daroca town as well as Miocene rocks close to it (sites 1 to 10 in Fig. 2A, Table 1). Multiple S and C planes were measured at six sites: four of them are located within the fault rocks of the hanging-wall block where the involved materials are predominantly microbreccias (sites 2, 3, 4 and 9 in Fig. 4); the other two belong to Middle Miocene rocks, either of the footwall block (site 6) or from the downthrown block of the extensional fault (likely representing those that formerly lapped onto the thrust front, as explained below; site 7). Both S and C planes mostly strike NW-SE, the C planes always dipping shallower than the S ones,

therefore indicating reverse shear with transport direction broadly oriented within the NE quadrant (see the corresponding stereoplots in Fig. 4). Nevertheless, certain variability is found within the data set, so that distinct local transport directions towards E (sites 3 and 6), NE (sites 2 and 9) and N (site 7) can be inferred. Fault striations directly measured on the main thrust plane in site 2 also record transport direction towards N and NNE.

Sites 11 and 12 are located at the upper part of the thrust ramp, in the northwestern sector (Fig. 2A). Materials involved in site 12 are microbreccia and foliated lutite close to the Cambrian-Miocene boundary, within a 1,2-m-thick fault rock band (see litho-structural transect in Fig. 3E). Site 11 corresponds to a thin slice of Cambrian shales within the hanging-wall block, bounded by the main thrust surface and a minor one above it. Both sites show S-C structures, indicating transport directions towards NE and E, respectively. Several fault striations were also measured in site 12 and two orientation maxima can be distinguished: the first maximum closely fits the NE-striking movement plane obtained from S-C structures, while the second one indicates a transport direction towards N and NNE (parallel to that observed in site 2).

Sites 14, 15 and 16 are located at the frontal footwall flat, in the northeastern sector (Figs. 2A and 3B, 3C). Data sites 14 and 15 are very close to each other and correspond to the first litho-structural transect represented in Fig. 3A, while site 16 is located in the second transect of Fig. 3A, some 5 m east of the former one. Both transects show up to 2-m-thick fault rock band (breccia, microbreccia and fault gouge), whose protoliths are Cambrian dolostones. A decrease of fragments size as approaching the main thrust surface can be broadly recognized along both transects. Independently of their size, rock fragments are strongly angular and show a preferred orientation that defines a penetrative foliation S. This foliation is accompanied by discrete C planes and, in site 16, also by sigmoid, decimeter-scale bodies of competent carbonate embedded within a micro-breccia matrix (Fig. 3A, close view in the second transect). Analysis of S-C relationships indicates a transport direction towards NNE in site 14, and close to E in sites 15 and 16 (see stereoplots in Fig. 3A). The sigmoid bodies have been interpreted as 'horses' making small-scale duplexes genetically related and kinematically consistent with the thrust movement. No fault striation has been observed in this sector of the thrust surface.

In summary, shear strain associated to thrusting within the Daroca fault zone appears as highly heterogeneous. Style and intensity of deformation strongly varies on a few meters along the fault

zone, and on a few centimeters or decimeters across the fault rock. Transport directions display a high variability, although almost of them are comprised within the NE quadrant.

Finally, we should refer to a set of extensional structures that overprint the contractive ones in some of the surveyed outcrops. First, meter-scale extensional shear bands occur at site 4, consistently striking NNW-SSE and dipping westwards (see corresponding stereoplot in Fig. 4). These bands locally show decimeter-scale spacing and internal foliation almost parallel to them, revealing a significant ductile component of deformation. In some cases, extensional bands sharply cut the thrust-related foliation (see hand specimen illustrated in Fig. 10A). But extensional shear seems also to be distributed at a metric scale in some zones, inducing reorientation of the previous S foliation. This could explain the systematic change in orientation of S surfaces between sites 2, 9, 3 and 4: as approaching the extensional shear bands at site 4, the strike of S planes progressively veers from NW-SE to NNW-SSE and N-S.

Other young extensional structures overprinting the reverse Daroca fault zone are brittle metre- to kilometre-scale faults. The largest one is the normal fault that makes the contact between the Palaeozoic rocks of the Daroca hanging-wall block and the Plio-Pleistocene materials of the Jiloca half-graben (Figs. 2A and 2B). The rest are metre- to decametre-scale ruptures observed and measured in Middle Miocene clastic rocks (sites 7 and 15), in Palaeozoic dolostones (sites 4 and 11), as well as in other neighbouring exposures as the one illustrated in Fig. 5A. All of these faults and fractures strike NNW-SSE in average (Fig. 5B).

5.2. Mineralogy of fault rocks and palaeothermal constraints

Fault rocks were mainly collected from the hanging-wall and footwall fault rocks associated with the thrust ramp South of Daroca town (in sites 1, 3 and 9). The former rocks are foliated clay-rich lithologies (samples HD1a, HD6a) or cataclasites (sample HD3c) that bound dolostone lithons, the latter are gouges (samples HD1b, HD1d, HD1f) and cataclasites (sample HD1c) derived from comminution of middle Miocene clastic rocks. Only sample HD11a is from microbreccias located at the frontal footwall flat (in site 13), which show strongly angular clasts and a preferred orientation defining a penetrative foliation (Table 2).

Whole rock composition of fault rocks at the hanging-wall of the Daroca thrust ramp consists mainly of phyllosilicates (75-82%), quartz (10-15%) and carbonate minerals (5-10%, calcite and dolomite). Hematite and gypsum occur as minor phases with contents that do not exceed 2% (Table 2). The <2 µm grain-size fraction shows an illite-rich composition (57-73%) and subordinate amounts of chlorite (11-36%) and mixed layers I-S (7-8%). Kaolinite was observed only in sample HD6a. Mixed illite-smectite layers are random ordered structures (R0) with low amounts of non-expandable layers (10%).

Fault rocks from the footwall are characterized by high amounts of phyllosilicate minerals (65-84%) followed by quartz (9-19%), calcite (2-25%) and very low contents of dolomite (1%). Hematite occurs with contents between 1% and 3% and traces amounts of goethite were occasionally observed (Tab. 1). X-ray patterns of the <2 µm grain size fraction show a mineralogical composition made up of illite (51-58%), chlorite (5-38%), kaolinite (5-30%) and mixed layers I-S (7-15%) that display R0 stacking order and an illite content between 10 and 20% (Table 2).

Sample HD11a (site 13) shows a mineralogical assemblage constituted by phyllosilicate minerals, quartz and low amounts of dolomite and calcite (Table 2). Among phyllosilicate minerals, illite (58%), kaolinite (19%), chlorite (12%) and mixed layers I-S (11%) are the main components of the <2 µm grain-size fraction. Mixed layers I-S display random ordered structures with an illite content of 10%.

The occurrence of highly expandable mixed layer I-S in both hanging-wall and footwall rocks indicate very shallow burial depths in early diagenetic conditions suggesting that deformation took place at depths lower than 2 km and at temperature of about 60-70°C consistent with the beginning of smectite-to-illite transition (Hoffman and Hower, 1979; Środoń, 1999). No evidence of fluid circulation within the fault zone, which could have induced mineralogical changes itself, has been found.

5.3. Magnetic mineralogy

AMS analysis of fault rocks in the Daroca area shows bulk magnetic susceptibility varying between $131x10^{-6}$ SI and $352x10^{-6}$ SI (Fig. 6B) with an average value of $226x10^{-6}$ SI.

Thermomagnetic (k-T) curves are analysed by means of the method of Hrouda *et al.* (1997). They are characterized by a hyperbolic decay of magnetic susceptibility at their initial part (40 to 300°C) in all cases, indicating that paramagnetic minerals (probably phyllosilicates) are carriers of the magnetic susceptibility (Fig. 7A). Curves from samples HD2-9a and HD3-3 (sites 2 and 3) are very similar to curve of sample HD10-3 (site 16), where other magnetic mineralogies cannot be recognized (Fig. 7A). In the other three analysed samples, the presence of ferromagnetic minerals can be recognized by sudden susceptibility drops around 675°C that is the Néel temperature of hematite (samples HD1, HD6-6 and HD9-12, Fig. 7A). In one of the samples, the curve shows a small increase and subsequent drop in magnetic susceptibility during heating around 280°C and 320°C respectively, that can be related to the local presence of iron sulphides (sample HD1, Fig. 7A). In all samples, curves are non-reversible, the cooling curve showing a conspicuous increase in susceptibility around 620°C and much higher susceptibilities in general, indicating the creation of new ferromagnetic phases at high temperatures.

Results of the thermal demagnetization of the natural remanent magnetization (NRM) indicate that the main ferromagnetic contributor to the NRM is a phase whose maximum unblocking temperature is near 670°C, probably hematite (Fig. 7B), accordingly to the results of thermomagnetic curves and whole rock composition of the fault rocks. Besides, AF demagnetizations were ineffective, as expected when a hard coercive carrier like hematite is present.

5.4. AMS results

Magnetic ellipsoids in the Daroca fault zone are dominantly oblate ($1 \geq T \geq 0$), although triaxial magnetic fabrics ($T \approx 0$) are measured in site 2, and prolate magnetic fabrics in site 16 (Table 3, Fig. 6C). The corrected anisotropy degree ranges between 1.031 and 1.079 (Table 3): fault microbreccias show the lowest P' values, whereas intermediate and higher anisotropy degree values were defined for the fault gouge. Considering the whole dataset (Fig. 6A), and despite a significant dispersion, k_{max} axes are nearly horizontal having a dominant NW-SE-trend, while k_{min} axes are scattered in a NE-SW-striking, nearly vertical girdle with an intermediate NE-plunging maximum. In general terms, magnetic lineation is nearly parallel to the strike of the Daroca fault while magnetic foliation strikes parallel to the fault although displaying variable dips.

When looking at the site-scale, the orientation of the magnetic ellipsoid varies along and across the fault zone (Table 4, Fig. 8). Near the contact with the footwall, the Daroca thrust strikes N130°E and dips shallowly (15°) to the South. Magnetic foliation in the fault rocks sampled in this domain is nearly horizontal (sites 1 and 3), or it strikes parallel to the Daroca thrust with intermediate dips (site 2). Magnetic lineations are usually defined from well clustered k_{max} axes and show a constant horizontal, NNW-SSE to NW-SE trending orientation (Fig. 8). Site 9 displays strongly scattered k_{max} axes, but also provides a NW-SE mean. It was initially sampled according to a standard procedure, collecting 8 cores from which a total of 8 samples were analysed, with an inconsistent result probably due to the coarse grain size of the microbreccia. Only from a minimum number of 66 cubic samples obtained from a hand specimen, acceptable averages both for magnetic lineation and foliation could be obtained. This suggests an influence of the number of analysed samples on the definition of the AMS axes, particularly in cases of unfavourable texture.

In the northern fault zone (footwall flat) the magnetic foliation strikes NE-SW, but the magnetic lineation preserves its dominant attitude: it is nearly horizontal and trends NW-SE (site 16, Fig. 8).

AMS at low temperature enhances the contribution of paramagnetic minerals, and comparison with AMS at room temperature allows determining the presence of subfabrics. In the two sites measured at LT, the LT/RT ratios between magnetic susceptibilities are 1.86 (site 8) and 3.03 (site 16). Ratios lower than 3.8 and above 1 indicate that both paramagnetic and ferromagnetic minerals behave as carriers of the AMS. The contribution of paramagnetic phases is probably higher in site 16 (where the higher LT/RT ratio was obtained) than in site 8, where haematite is present, as indicated by the drop at 680°C in the thermomagnetic curve (Fig. 7A). The orientation of the magnetic ellipsoid at low temperature overlaps AMS at room temperature (Table 5, Fig. 9), indicating that the paramagnetic contribution dominates RT-AMS in both sites or, alternatively, paramagnetic and ferromagnetic contributions have the same fabric.

6. Interpretation and discussion

In this section we analyse the representativity of data and the meaning of AMS axes orientations in relation to foliations and transport directions within fault zones. According to the above-

exposed results, the kinematics of the Daroca thrust and its relationships with the overall structure of the area will be discussed.

6.1. Relationship between AMS and deformation: reliability of AMS as a kinematic indicator

Several elements must be taken into account when considering the relationships between tectonic and magnetic fabrics: (i) magnetic mineralogy, (ii) grain size relative to the AMS sample size, (iii) representativeness of the structural elements measured in the field, (iv) superposition of different tectonic stages and v) strain partitioning at different scales.

These relationships have been explored by using three different approaches. The first one was a detailed AMS analysis of a decimetre-scale specimen collected in site 2 (Fig. 10). Within it, the compressional foliation S is cut by a steeply-dipping shear band (ESB in Fig. 10A) related to Pliocene extensional deformation. At a microscopic scale, the compressional fabric is expressed by (i) undulate, discontinuous solution surfaces, and (ii) angulose, heterogeneously sized and roughly oriented fault-rock fragments (Fig. 10B). These textural features suggest that pressure-solution and cataclastic flow are the prevailing deformation mechanisms. C planes are virtually absent in both the hand sample and thin sections, although they could be observed as meso-scale surfaces in the nearest outcrop. A total of 68 specimens were measured for AMS determination, thus intensifying subsampling with respect to the standard procedure, as made for site 9. The results indicate that the magnetic foliation is parallel to the foliation observed in the sample (Fig. 10C and D). This includes both the compressional foliation dipping about 40°S and the more discontinuous, extensional foliation. The magnetic lineation is nearly horizontal and parallel to the intersection line between S and C planes, and therefore orthogonal to the transport direction.

Our second approach was a site-by-site comparison of the AMS and the structural markers in other data sites where both types of information are available (sites 2, 3, 9 and 16). In all cases, the magnetic lineation approaches the average intersection line between meso-scale S and C planes (see the corresponding stereoplots in Fig. 8 compared with those in Figs. 3A and 4), i.e. the same orientation pattern described for sample HD2. Concerning the relationship between the magnetic foliation and the meso-scale S foliation, it is not fully consistent: both are nearly parallel to each

other in sites 2, while they are oblique in site 3 and 9 (similar NW-SE strike but opposite sense of dip), and the magnetic foliation roughly parallels the average C plane in site 16.

Finally, the third approach considers the whole mesostructural and AMS datasets, which can be graphically compared by means of synthetic stereoplots (Fig. 11). In spite of their strong variability, the relationships previously described in individual sites are corroborated by the overall data. Nevertheless, such relationships appear as slightly different depending on the procedure used for averaging the orientation of the AMS vectors: either as vectors k_{maxM}, k_{intM} and k_{minM} of the mean AMS tensor obtained from the ensemble of 189 analysed specimens (Fig. 11A), or as a mean orientation of the local vectors (k_{maxL}, k_{intL} and k_{minL}) obtained at the six AMS sites (Fig. 11B). After comparing with the synthetic stereoplot of mean poles to S and C planes, obtained from the site means (Fig. 11C), it can be seen that: (i) the magnetic foliation averaged from the overall data (k_{minM} axis parallel to the mean S pole) closely parallels the mean S foliation; (ii) the magnetic foliation defined as the mean orientation of local vectors k_{maxL}, k_{intL} and k_{minL} shows an intermediate orientation between the mean S and C planes (Fig. 11D); (iii) the magnetic lineation (k_{max}) runs at high angle to the transport direction (therefore close to the S-C intersection line) in every case (Fig. 11E).

From the previous partial observations the following general relationships are inferred:

(1) The magnetic foliation shows a double tendency to parallelize either the meso-scale S foliation, or the C planes (Fig. 11D). This suggests that shear planes also contribute to the attitude of magnetic foliation, because of either re-orientation of phylosillicates or concentration of preferentially oriented ferro-magnetic minerals (mostly hematite). Magnetic foliation at an intermediate position between S and C planes has been described in other fault zones, both under extensional and compressional regimes (Aranguren *et al.*, 1996; Casas *et al.*, 2017).

(2) The magnetic lineation makes a high angle to the transport direction. Overall considered, the most representative transport direction (towards NE to NNE, consistent with the movement plane M obtained from the whole S-C data, Fig. 11C, and so with the macrostructural trend) is nearly orthogonal to the magnetic lineation (k_{maxM} and k_{maxL} in Fig. 11E). It is true that other transport directions towards E and N are recorded in structural data. The reality of such multiple movements is evinced in site 12 by superposition of two slickenlines distinctly oriented indicating successive transport towards NNE and N (Fig. 3). In spite of such kinematic heterogeneity,

comparing site-by-site four cases in which both AMS and thrust kinematics have been established (sites 2, 3, 9, 16), the angles between transport direction and the corresponding k_{max} axis are consistently high, in the range of 53° to 82° (Fig. 11E). Such relationships can be explained from both deformational and mineralogical controls. Where the magnetic lineation is mainly defined by paramagnetic carriers, it evolves from parallelism to the S-C intersection line during earlier deformational stages (i.e. linked to low finite shear strain, which would be our case) to parallelism to the transport direction in advanced stages (Parés *et al.,* 1999; Pueyo *et al.*, 2010). Where the magnetic lineation relates to ferromagnetic carriers, it generally parallels the transport direction (Casas *et al.*, 2017; Oliva *et al*., 2009). In our case, the low ferromagnetic contribution to susceptibility can explain why the magnetic lineation has remained orthogonal or makes a high angle to the transport direction.

6.2. Kinematics of the Daroca thrust from structural, palaeothermal and magnetic data

Based on the above-exposed interpretations of the results coming from the different techniques, we can propose a kinematic interpretation of the Daroca thrust. As an average, a NE-directed reverse movement and a shallow depth for deformation can be inferred. However, different transport directions coexist, as inferred both from AMS analysis and kinematic indicators, and a strongly heterogeneous deformation has been noticed across the studied fault rock bodies. Are these variations along the fault zone a result of random heterogeneity of strain or do they rather respond to actually changing movements during the compressional stage and/or strain partitioning within the fault zone? To evaluate a satisfying hypothesis several issues should be considered and discussed:

1) The coexistence of different transport directions, either sequential (successive tectonic episodes) or simultaneous (strain partitioning). From the overall kinematic data, two prevailing transport directions have been inferred, towards NNE and E, respectively. The interpretation of sequential movements is consistent with the notion of the Daroca thrust as an inherited Late-Variscan fault, although in this case it would be difficult to differentiate between Permian or Mesozoic movements and its displacement during the Cenozoic. Furthermore, the mineralogy of the fault zone and the derived paleothermal estimates rather point to a shallow (hence late,

Cenozoic) origin for the fault zone. The coincidence between transport directions recorded in the Aragonian deposits and the damaged fault zone also supports the notion of a thrust mainly active during the Cenozoic time. Temporal heterogeneity of Alpine compressional stress fields (Capote *et al.,* 2002; Liesa and Simón, 2009), therefore acting at different angles with respect to the inherited thrust surface, probably gave rise to distinct, successive transport directions. Such scenario has been accurately reported in other thrust sheets within the Iberian Chain (Utrillas thrust, Simón and Liesa, 2011). Also, strain partitioning can be invoked for explaining the kinematic variability noticed within the rock fault band, in the light of the transpressional model commonly applied to the overall NW-SE trending structures in the central Iberian Chain (Casas *et al.,* 1998; De Vicente *et al.,* 2009) and, specifically, to the Daroca fault zone (existence of E-W striking, *en-échelon* segments: Colomer, 1987; Colomer and Santanach, 1988). According to that model, simultaneous movements with different vectors on the ramp and the flat zones of the thrust, as well as on the deep, master fault are feasible, as a result of partitioning of the overall transpressional deformation into strike-slip and reverse slip components (Elías-Herrera and Ortega-Gutiérrez, 2002; Sarkarinejad and Azizi, 2008; Sarkarinejad *et al.,* 2008; McCaffrey, 2009). Furthermore, the epiglyptic character of the thrust could also favour the existence of variable transport directions on the frontal flat controlled by topographic slope.

The kinematic evolution of the Daroca fault zone could be even more complex if we take into account the possibility of a further compressional stress field oriented close to E-W (the so called *Altomira compression* in regional models of Cenozoic stress evolution: Muñoz and De Vicente, 1998; Simón and Liesa, 2011). It is recorded in Lower-Middle Miocene materials of the Mijares and southern Teruel basins (Simón and Paricio, 1988), and it could also explain the eastwards transport directions here reported for the Daroca thrust. If such E-W remote compression was active during the Early-Middle Miocene, the Daroca fault zone could undergo a hypothetic sinistral movement in addition to the dominant dextral one.

2) The existence of post-Miocene extensional shear zones has contributed to deflect the main compressional S foliation. Extensional meso-scale faults are consistently oriented NNW-SSE, parallel to the younger shear bands (Figs. 5 and 10). Moreover, they are also parallel to the regional trend of the most recent extensional structures in the whole central-eastern Iberian Chain, and orthogonal to the dominant trend (ENE-WSW) of σ_3 trajectories representing the Plio-Pleistocene extensional stress field (Simón-Gómez, 1989; Arlegui *et al.,* 2005). Therefore, we attribute all the described extensional structures to the late Neogene extensional tectonics that

gave rise to negative inversion of the Daroca fault zone. If the hypothesis of reorientation of the compressional S foliation by those NNW-SSE trending extensional structures was true, we should consider critically the reliability of the kinematical results obtained from sites in which the S planes strike close to NNW-SSE. Maybe the nearly eastwards transport directions obtained from those S-C data sets do not represent the true original directions, and these should be interpreted as being closer to NE or NNE.

3) Finally, we should critically evaluate the representativeness of the available data. The necessarily discontinuous sampling, the limited outcropping areas and the poor accessibility to the exposures make difficult a statistically representative sampling (which is intrinsic to many geological works indeed). In our case, the subsequent sampling of hand specimens in areas where magnetic fabrics or petrofabrics were poorly defined has allowed for a better characterization of both foliations and lineations.

In summary, there are several feasible explanations for the variability of orientation of fabrics in the Daroca thrust, some of them related to intrinsic factors (grain size of fault rock, high number of discontinuities, etc.) and others to extrinsic factors (mainly variations in strain intensity and shortening direction).

6.3. The origin of the Daroca thrust: geometrical constraints

We have described (Section 3) the structure of the Palaeozoic sequence south of the Calatayud basin as a large-scale monocline dipping 45° to 55°S. According to the geometric reconstruction (Fig. 12A), the Daroca thrust is probably parallel to the average bedding within the Cambrian series. The occurrence of Lower Triassic materials dipping 15°S and overthrust by Cambrian units along a bedding-parallel rupture surface can be observed in several points along the Palaeozoic monocline (e.g. Manchones-Murero area; Gabaldón, 1983). This gives a clue about a possible mechanism for the formation of the Daroca thrust through re-activation of flexural-slip folds (Alonso, 1987; Casas *et al.*, 2000). An increase in dip of 15° (from 30° to 45°S; Fig. 12B) of a 1750 m thick sequence (Lower Cambrian) could explain the observed structure of the Daroca thrust. The accommodation space created by the thrust displacement allowed for more than 500 m of sediments to be accumulated in this sector of the Calatayud basin, and the tip of the thrusting sheet could be folded depending on the uplift/sedimentation ratio. It is important to note that this model only accounts for the vertical displacement of the Daroca thrust. Horizontal displacements

resulting from the obliquity of the shortening direction with respect to the initial strike of the Palaeozoic series could also be added, thus defining a transpressional setting for the Daroca thrust.

The other end-member model for the origin of the Daroca thrust would be a nearly-vertical, NW-SE striking Late-Variscan fault (Alvaro *et al.*, 1979) cutting across the whole Palaeozoic series and undergoing transpressional deformation during the Alpine Orogeny (Fig. 12C). In this case the formation of the Daroca thrust would be related to a positive, asymmetric flower structure, vertical at depth (rooted in that Late-Variscan fault) and nearly horizontal in its surface expression; some of the cataclasis of the Cambrian dolostones would be then probably related to strike-slip Permian faulting. Both models account for the epiglyptic displacement of the thrust front and involve horizontal tilting of the frontal segment of the hanging-wall.

In either of the described models, additional, late folding could involve the whole structure, resulting in the forelandwards dip of both the thrust front and the Miocene materials of the footwall block (see the last stages in Fig. 12B and C).

7. Conclusions

The Daroca thrust and its fault damage zone offer an invaluable natural laboratory for testing the applicability of magnetic methods to the analysis of fault zones in intraplate settings.

The results indicate that robust means can be obtained provided that the density of sampling sites is in correspondence with the heterogeneity and grain size of the fault rock. The minimum number of samples necessary to determine a reliable solution increases as the grain size of the microbreccia increases. The possibility of averaging the magnetic lineation over a large number of samples is an added value for the application of AMS to the study of fault rocks for regional or general evaluations. This applies even when orientation of structures cannot be clearly determined from outcrop observations.

Regarding the correspondence between AMS and structural indicators, the attitude of the dominant magnetic foliation is either parallel to the compressional foliation (S planes) or at an intermediate orientation between S and C planes. The magnetic lineation is parallel to the intersection lineation between S and C planes and therefore perpendicular to the transport

direction. Variability in orientation of the magnetic fabric reveals the heterogeneity of the fault zone associated with the Daroca thrust, probably resulting from strain partitioning and sequential movements.

The Daroca thrust can be characterized as a reverse fault having a minimum throw of 500 m during the Early-Middle Miocene and developed at shallow depths. The change in geometry of the fault zone (from footwall ramp to footwall flat) is recorded by differences in thickness of the damage zone. Younger normal displacements (Neogene in age) contribute to the deflection of the contractive S fabric of fault rocks and to the development of new shear zones.

The results obtained in this work have relevant implications, especially regarding the utility of AMS for studying fault rocks. AMS can therefore be added to classical structural analysis and crystallographic orientations (e.g. Woodcock and Rickards, 2003; Toy *et al.*, 2008) to search strain geometry and kinematics. Interpretations of fault kinematics and driving mechanisms of intra-plate deformation, including fault reactivation under transpression/transtension mechanisms (e.g. Hippolyte, 2002; van Hinsbergen *et al.*, 2015; Giamboni *et al.*, 2004), or active, potentially seismogenic faults (Lavenu and Cembrano, 1999; Cunningham, 2005; Pedrera *et al.*, 2013) can in this way benefit from analysis of magnetic anisotropy.

Acknowledgements

Authors acknowledge the use of Servicio General de Apoyo a la Investigación-SAI, Universidad de Zaragoza (Servicio de Preparación de Rocas y Materiales Duros and Servicio de Líquidos Criogénicos) and thank Sylvia Gracia for her help in AMS measurements, and Juan José Villalaín for the use of the palaeomagnetic laboratory of the Burgos University. This study has been financed by the research project UZ2012-CIE-11 of the University of Zaragoza and the research projects CGL2013-42670-P and CGL2012-35662 of the MINECO (Ministerio de Economía y Competitividad of Spain). The authors thank Rob Govers, Charles Aubourg and an anonymous reviewer for constructive revisions, who helped to improve a former version of the manuscript.

References

Aldega, L., Botti, F. & Corrado, S. 2007. Clay mineral assemblages and vitrinite reflectance in the Laga Basin (Central Apennines, Italy): What do they record? *Clays and Clay Minerals*, **55**, 504–518.

Aldega, L., Corrado, S., Di Paolo, L., Somma, R., Maniscalco, R. & Balestrieri, M. L. 2011. Shallow burial and exhumation of the Peloritani Mts. (NE Sicily, Italy): Insight from paleo-thermal and structural indicators: Geological Society of America Bulletin, **123**, 132-149.

Aldega, L., Corrado, S., Carminati, E., Shaban, A. & Sherkati, S. 2014. Thermal evolution of the Kuh-e-Asmari and Sim anticlines in the Zagros fold-and-thrust belt: implications for hydrocarbon generation. *Marine and Petroleum Geology*, **57**, 1-13.

Aldega, L., Carminati, E., Scharf, A., Mattern, F. & Al-Wardi, M. 2017. Estimating original thickness and extent of the Semail Ophiolite in the eastern Oman Mountains by paleothermal indicators. *Marine and Petroleum Geology,* **84**,18-33.

Allmendinger, R. W., Cardozo, N. C. & Fisher, D. 2013. Structural geology algorithms: vectors & tensors. Cambridge University Press, Cambridge.

Alonso, J. L. 1987. Sequences of thrusts and displacement transfer in the superposed duplexes of the Esla Nappe Region (Cantabrian Zone, NW Sapin). *Journal of Structural Geology*, **9**, 969-983.

Alvaro, M. 1991. Tectónica. In: Mapa Geológico de Daroca 1:200.000. *Instituto Tecnológico GeoMinero de España*, **40** (7-5), 177-204.

Alvaro, M., Capote, R. & Vegas, R. 1979. Un modelo de evolución geotectónica para la Cadena Celtibérica. *Acta Geológica Hispánica*, **14**(1), 172-177.

Alvaro, J. J. & Zamora, S. 2011. The Lower Ordovician of the Iberian Chains, NE Spain. 11th ISOS, Ordovician of the Iberian Range (NE Spain) Post Symposiym field trip, 24-31.

Ansón, M., Gil., A. & Simón, J. L. 2017. Las rocas de falla del cabalgamiento de Daroca (sector central de la Cordillera Ibérica): interpretación reológica y cinemática. *Geogaceta*, **61**, 75-78.

Aranguren, A., Cuevas, J. & Tubía, J. M. 1996. Composite magnetic fabrics from S-C mylonites. *Journal of Structural Geology, 18*, 863-869.

Arlegui, L. E., Simón, J. L., Lisle, R. J. & Orife, T. 2005. Late Pliocene-Pleistocene stress field in the Teruel and Jiloca grabens (eastern Sapin): contribution of a new method of stress inversion. *Journal of Structural Geology*, **27** (4), 693-705.

Arthaud, F. & Matte, P. 1975. Les décrochements tardi-hercyniens du Sud-Ouest de l'Europe. Géométrie et essai de reconstitution des conditions de la déformation. *Tectonophysics*, **25**(1), 139-171.

Arthaud, F. & Matte, P. 1977. Late Paleozoic strike-slip faulting in southern Europe and northern Africa: Result of a right-lateral shear zone between the Appalachians and the Urals. *Geological Society of America Bulletin*, **88**(9), 1305-1320.

Balsamo, F., Aldega, L., De Paola, N., Faoro, I. & Storti, F. 2014. The signature and mechanics of earthquake ruptures along shallow creeping faults in poorly lithified sediments. *Geology*, **42**, 435-438.

Ben-Zion, Y. & Sammis, C. G. 2003. Characterization of fault zones. *Pure and Applied Geophysics*, **160**(3-4), 677-715.

Billi, A. & Storti, F. 2004. Fractal distribution of particle size in carbonate cataclastic rocks from the core of a regional strike-slip fault zone. *Tectonophysics*, **384**(1-4), 115-128.

Braun, D., Weinberger, R., Eyal, Y., Feinstein, S., Harlavan, Y. & Levi, T. 2015. Distinctive diamagnetic fabrics in dolostones evolved at fault cores, the Dead Sea Transform. *Journal of Structural Geology*, **77**, 11-26.

Calvín-Ballester, P. & Casas, A. 2014. Folded Variscan thrusts in the Herrera unit of the Iberian Range (NE Spain). *Geological Society, London, Special Publications*, **394**(1), 39-52.

Capote, R., Muñoz, J. A., Simón, J. L., Liesa, C. L. & Arlegui, L. E. 2002. Alpine Tectonics I: The Alpine system north of the Betic Cordillera. In: Gibbons, W., Moreno, T. (Eds)*, Geology of Spain*, The Geological Society, London, 367-400.

Cardozo N. & Allmendinger R. W. 2013. Spherical projections with OSXStereonet. *Comput Geosci,* **51**, 193-205.

Caricchi, C., Aldega, L. & Corrado, S. 2015. Reconstruction of maximum burial along the Northern Apennines thrust wedge (Italy) by indicators of thermal exposure and modeling. *Geological Society of American Bulletin,* **127** (3-4), 428-442.

Carlini, M., Artoni, A., Aldega, L., Balestrieri, M. L., Corrado, S., Vescovi, P., Bernini, M. & Torelli, L. 2013. Exhumation and reshaping of far-travelled/allochthonous tectonic units in mountain belts. New insights for the relationships between shortening and coeval extension in the western Northe rn Apennines (Italy). *Tectonophysics,* **608**, 267–287.

Carls, P. 1991. Datos cartográficos inéditos del Paleozoico. In: Mapa Geológico de Daroca 1:200.000. *Instituto Tecnológico GeoMinero de España,* **40** (7-5).

Carminati, E., Aldega, L., Bigi, S., Corrado, S., D'Ambrogi, C., Mohammadi, P., Shaban, A. & Sherkati, S. 2013. Control of Cambrian evaporites on fracturing in fault-related anticlines in the Zagros fold-and-thrust belt. *International Journal of Earth Sciences*, **102**, 1237-1255.

Carminati, E., Aldega, L., Bigi, S., Minelli, G. & Shaban, A. 2016. Not so simple "simply-folded Zagros": the role of pre-collisional extensional faulting, salt tectonics and multi-stage thrusting in the Sarvestan transfer zone (Fars, Iran). *Tectonophysics*, **671**, 235-248.

Casas, A.M., Cortés, A.L., Gapais, D., Nalpas, T. & Román-Berdiel, T. 1998. Modelización analógica de estructuras asociadas a compresión oblicua y transpresión. Ejemplos del NE penindular. *Revista de la sociedad Geológica de España*, **11**(3-4), 331-344

Casas, A. M., Cortés-Gracia, A. L. & Maestro-González, A. 2000. Intraplate deformation and basin formation during the Tertiary within the northern Iberian plate: Origin and evolution of the Almazán Basin. *Tectonics,* **19** (2), 258-289.

Casas Sainz, A. M. & Faccenna, C. 2001. Tertiary compressional deformation of the Iberian plate. *Terra Nova*, **13**(4), 281-288.

Casas-Sainz, A. M., Román-Berdiel, T., Oliva-Urcia, B., García-Lasanta, C., Villalaín, J. J., Aldega, L., Corrado, S., Caricchi, C., Invernizzi, C. & Osácar, M. C. 2017. Multidisciplinary approach to constrain kinematics of fault zones at shallow depths: a case study from the Cameros–Demanda thrust (North Spain). *International Journal of Earth Sciences*, **106**, 1023-1055.

Casas-Sainz, A. M. & Cortés-Gracia, A. L. 2002. Cenozoic landscape development within the central Iberian Chain, Spain. *Geomorphology*, **44**(1), 19-46.

Chadima, M. & Hrouda, F. 2009. Cureval 8.0: Thermomagnetic Curve Browser for Windows. *Agico, Inc.*

Chadima, M. & Jelinek, V. 2009. Anisoft 4.2: Anisotropy Data Browser for Windows. *Agico, Inc.*

Chou, Y.-M., Song, S.-R., Aubourg, C., Lee, T.-Q., Boullier, A.-M., Song, Y.-F., Yeh, E.-C., Kuo, L.-W. & Wang, C.-Y. 2012a. An earthquake slip zone is a magnetic recorder. *Geology,* **40**, 6, 551-554.

Chou, Y.-M., Song, S.-R., Aubourg, C., Song, Y.-F., Boullier, A.-M., Lee, T.-Q., Evans, M., Yeh, E.-C. & Chen, Y.-M. 2012b. Pyrite alteration and neoformed magnetic minerlas in the fault zone of the Chi-Chi earthquake (Mw7.6, 1999): Evidence for frictional heating and co-seismic fluids. Geochemistry, Geophysics, Geosystems: G3, 13, 8.

Chou, Y.-M., Song, S.-R., Aubourg, C., Lee, T.-Q., Song, Y.-F. and Yeh, E.-C. 2014. Quantitative modeling of the newly formed magmatic minerals in the fault gouge of 1999 Chi-chi earthquake (Mw 7.6), Taiwan. *Journal of Geophysical research: Solid Earth*, **119,** 9, 6771-6781.

Colomer, M. 1987. *Estudi geològic de la vora Sud-oest de la Fossa de Calatayud-Daroca entre Villafeliche i Calamocha*. MSc Thesis, University of Barcelona, 99 pp.

Colomer, M. & Santanach, P. 1988. Estructura y evolución del borde sur-occidental de la Fosa de Calatayud-Daroca. *Geogaceta*, **4**, 29-31.

Corrado, S., Aldega, L. & Zattin M. 2010. Sedimentary vs. tectonic burial and exhumation along the Apennines (Italy). *Journal of the Virtual Explorer*, **36**, doi:10.3809/jvirtex.2009.00232.

Cortés-Gracia, A. & Casas-Sainz, A. M. 1996. Deformación alpina de zócalo y cobertera en el borde norte de la Cordillera Ibérica (Cubeta de Azuara-Sierra de Herrera). *Revista de la Sociedad Geológica de España,* **9** (1-2), 51-66.

Cunningham, D. 2005. Active intracontinental transpressional mountain building in the Mongolian altai: Defining a new class of orogen. *Earth and Planetary Science Letters*, **240**, 436-444.

De Vicente, G., Cloetingh, S. A. P. L., Van Wees, J. D. & Cunha, P. P. 2011. Tectonic classification of Cenozoic Iberian foreland basins. *Tectonophysics*, ***502***(1), 38-61.

De Vicente, G., Vegas, R., Muñoz-Martín, A., Van Wees, J. D., Casas-Sáinz, A., Sopeña, A., Sánchez-Moya, Y., Arche, A., López-Gómez, J. & Olaiz, A. 2009. Oblique strain partitioning and transpression on an inverted rift: The Castilian Branch of the Iberian Chain. *Tectonophysics*, **470**(3), 224-242.

De Vicente, G. 2004. Estructura alpina del Antepaís Ibérico. In: J.A. Vera (Ed.), Geología de España. *SGE-IGME*, 587-634.

De Vicente, G., Vegas, R., Muñoz-Martín, A., Silva, P. G., Andriessen, P., Cloetingh, S., González-Casado, J. M., Van Wees, J. D., Álvarez, J., Carbó, A. & Olaiz, A. 2007. Cenozoic thick-skinned and topography evolution of the Spanish Central System. *Glob. Planet. Change,* **58***,* 335–381.

Di Paolo, L., Aldega, L., Corrado, S. & Mastalerz, M. 2012. Maximum burial and unroofing of Mt. Judica recess area in Sicily: Implication for the Apenninic-Maghrebian wedge dynamics. *Tectonophysics*, **530-531**, 193-207.

Dunlop, D. J. & Özdemir, Ö. 1997. Rock Magnetism. Fundamentals and frontiers. *In*: Edwards, D., Ed., Cambridge Studies in Magnetism. *Cambridge University Press*, 253 pp.

Dyksterhuis, S. & Müller, R. D. 2008. Cause and evolution of intraplate orogeny in Australia. *Geology*, 36(6), 495-498.

Elías-Herrera, M. & Ortega-Gutiérrez, F. 2002. Caltepec fault zone: An Early Permian dextral transpressional boundary between the Proterozoic Oaxacan and Paleozoic Acatlán complexes, southern Mexico, and regional tectonic implications. *Tectonics*, **21**(3).

Faulkner, D. R., Lewis, A. C. & Rutter, E. H. 2003. On the internal structure and mechanics of large strike-slip fault zones: field observations of the Carboneras fault in southeastern Spain. *Tectonophysics*, **367**(3-4), 235-251.

Fernández-Lozano, J., Sokoutis, D., Willingshofer, E. D., Cloetingh, S. A. P. L. & De Vicente, G. 2011. Cenozoic deformation of Iberia: A model for intraplate mountain building and basin development based on analogue modeling. *Tectonics*, **30**(1).

Fisher, R. A. (1953). Dispersion on a sphere. *Proceedings of the Royal Society of London, A, 217*, 295-305.

Gabaldón, V (1983). Mapa Geológico de España, E. 1:50000 DAROCA. Instituto Geológico y Minero de España.

Gabrielsen, R. H., Odinsen, T. & Grunnaleite, I. 1999. Structuring of the Northern Viking Graben and the Møre Basin; the influence of basement structural grain, and the particular role of the Møre-Trøndelag Fault Complex. *Marine and Petroleum Geology*, **16**(5), 443-465.

Giamboni, M., Ustaszewski, K., Schmid, S.M., Schumacher, M.E. & Wetzel, A. 2004. Plio-Pleistocene transpressional reactivation of Paleozoic and Paleogene structures in the Rhine-Bresse transform zone. *International Journal of Earth Science*, **93**, 207-223.

Gracia, J. 1992. Tectónica pliocena de la Fosa de Daroca (prov. de Zaragoza). *Geogaceta*, **11**, 127–129.

Guimerà, J. & Alvaro, M. 1990. Structure et évolution de la compression alpine dans la Chaîne Ibérique et la Chaîne côtière catalane (Espagne). *Bull. Soc. Géol. Fr*, **8**, 339-348.

Gutiérrez, F., Gutiérrez, M., Gracia, F. J., McCalpin, J. P., Lucha, P. & Guerrero, J. 2008. Plio-Quaternary extensional seismotectonics and drainage network development in the central sector of the Iberian Range (NE Spain). *Geomorphology,* **102**, 21-42.

Gutiérrez, F., Gracia, F. J., Gutiérrez, M., Lucha, P., Guerrero, J., Carbonel, D. & Galve, J. P. 2012. A review on Quaternary tectonic and nontectonic faults in the central sector of the Iberian Chain, NE Spain/Fallas cuaternarias tectónicas y gravitacionales en el sector central de la Cordillera Ibérica, NE de España. *Journal of Iberian Geology*, **38**(1), 145.

Hippolyte, J.-C. 2002. Geodynamics of Dobrogea (Romania): new constraints on the evolution of the Tornquist-Teisseyre Line, the Black Sea and the Carpathians. *Tectonophysics*, **357**, 33-53.

Hirt, A.M. & Gehring, A. 1991. Thermal alteration of the magnetic mineralogy in ferruginous rocks. *J. Geophs. Res.,* **96**, 9947-9954.

Hoffman, J. & Hower, J. 1979. Clay mineral assemblages as low grade metamorphic geothermometers—Application to the thrust faulted disturbed belt of Montana, USA, in: Scholle, P.A., and Schluger, P.S., eds., *Aspects of Diagenesis*, Society of Economic Paleontologists and Mineralogists Special Publication **2**, 55-79.

Hrouda, F., Jelinek, V. & Zapletal, K. 1997. Refined technique for susceptibility resolution into ferromagnetic and paramagnetic components based on susceptibility temperature-variation measurement. *Geophys. J. Int.*, **129**: 715–719.

Izquierdo-Llavall, E., Aldega, L., Cantarelli, V., Corrado, S., Gil-Peña, I., Invernizzi, C. & Casas-Sainz, A. 2013. On the origin of cleavage in the Central Pyrenees: Structural and paleo-thermal study. *Tectonophysics*, **608**, 303–318.

Jagodzinski, H. 1949. Eindimensionale Fehlordnung in Kristallen und ihr Einfluss auf die Röntgen Interferenzen. *Acta Crystallographica,* **2**, 201-207.

Jelinek, V. 1978. Statistical processing of anisotropy of magnetic susceptibility measured on groups of specimens. *Studia Geophysica et Geodetica,* **22**, 50–62.

Jelinek, V. 1981. Characterization of the magnetic fabric of rocks. *Tectonophysics,* **79**, 63-70.

Julivert, M. 1954. Observaciones sobre la tectónica de la Depresión de Calatayud. *Arrahona* (publ. Museo de Sabadell), 3-18.

Keskineva, A., Georgiev, N., Naydenov, K., Jordanova, N., Jordanova, D. & Dimowa, L. 2016. Magneto-structural and mineralogical study of tectonic gouge. Bulgarian Geological Society, *National Conference with international participation "Geosciences 2016"*, 89-90.

Kley J. & Voigt T. 2008. Late Cretaceous intraplate thrusting in central Europe: effect of Africa–Iberia–Europe convergence, not Alpine collision. *Geology,* **36**(11), 839–842.

Lavenu, A. & Cembrano, J. 1999. Compressional- and transpressional-stress pattern for Pliocene and Quaternary brittle deformation in fore arc and intra-arc zones (Andes of Central and Southern Chile). *Journal of Structural Geology*, **21**, 1669-1691.

Levi, T., Weinberger, R. & Marco, S. 2014. Magnetic fabrics induced by dynamic faulting reveal damage zone sizes in soft rocks, Dead Sea basin. *Geophys. J. Int.,* **199**, 1214-1229.

Liesa, C. L. & Simón, J. L. 2009. Evolution of intraplate stress fields under multiple remote compressions: The case of the Iberian Chain (NE Spain). T*ectonophysics*, **474**, 144-159.

Lüneburg, C. M., Lampert, S. A., Hermann, I., Lebit, D., Hirt, A. M., Casey, M. & Lowrie, W. 1999. Magnetic anisotropy, rock fabrics and finite strain in deformed sediments of SW Sardinia (Italy). *Tectonophysics,* **307**, 51-74.

Mattauer, M. 1973. Les déformations des matériaux de l'écorce terrestre. Paris: Hermann, 493.

McCaffrey, R. 2009. The tectonic framework of the Sumatran subduction zone. *Annual Review of Earth and Planetary Sciences*, **37**, 345-366.

Meghraoui, M. & Pondrelli, S. 2012. Active faulting and transpression tectonics along the plate boundary in North Africa. *Annals of Geophysics*, **55**, 5, doi: 10.4401/ag-4970

Meneghini, F., Botti, F., Aldega, L., Boschi, C., Corrado, S., Marroni, M. & Pandolfi, L. 2012. Hot fluid pumping along shallow-level collisional thrusts: the Monte Rentella Shear Zone, Umbria Apennine, Italy. *Journal of Structural Geology*, **37**, 36-52.

Moore, D.M. & Reynolds, R.C. Jr. 1997. X-Ray Diffraction and the identification and analysis of clay minerals. Oxford, UK, Oxford University Press, 378 pp.

Moreno, E., Homberg, C., Schnyder, J., Person, A., du Peloux, A. & Dick, P. 2014. Fault imprint in clay units: magnetic fabric, structural and mineralogical signature. *EGU General Assembly* 2014. *Geophysical Research Abstracts*, **16**, EGU2014-15479.

Muñoz, A. & De Vicente, G. 1998. Origen y relación entre las deformaciones y esfuerzos alpinos de la zona centro-oriental de la Península Ibérica. *Revista de la Sociedad Geológica de España,* **11**, 57–70.

Oliva-Urcia, B., Larrasoaña, J. C., Pueyo, E. L., Gil., A., Mata, P., Parés, J. M., Schleicher, A. M. & Pueyo, Ó. 2009. Disentangling magnetic subfabrics and their link to deformation processes in cleaved sedimentary rocks from the Internal Sierras (west central Pyrenees, Spain). *Journal of Structural Geology,* **31** (2), 163-176.

Oliva-Urcia, B., Román-Berdiel, T., Casas, A.M., Pueyo, E.L. & Osácar, C. 2010. Tertiary compressional overprint on Aptian-Albian extensional magnetic fabrics, North Pyrenean Zone. *Journal of Structural Geology,* **32**, 362-376.

Otto, V. 2003. Inversion-related features along the southeastern margin of the North German Basin (Elbe Fault System). *Tectonophysics*, **373**(1), 107-123.

Parés, J.M., Van der Pluijm, B. & Dinarés-Turell, J. 1999. Evolution of magnetic fabrics during incipient deformation of mudrocks (Pyrenees, northern Spain). *Tectonophysics,* **307**, 1-14.

Parés, J.M. & Van der Pluijm B. A. 2002. Phyllosilicate fabric characterization by Low-Temperature Anisotropy of Magnetic Susceptibility (LT-AMS). *Geophys. Res. Lett.,* **29** (24), doi:10.1029/2002GL015459

Pedrera, A., Ruiz-Constán, A., Marín-Lechado, C., Galindo-Zaldívar, J., Gonzalez, A. & Peláez, J. A. 2013. Seismic transpressive basement faults and monocline development in a foreland basin (Eastern Guadalquivir, SE Spain). *Tectonics*, **32**, 1571-1586.

Pomella, H. 2014. Magnetic fabric of brittle fault rocks. *EGU General Assembly 2014. Geophysical Research Abstracts,* **16**, EGU2014-12505.

Pueyo Anchuela, O., Gil Imaz, A. & Pocoví Juan, A. 2010. Significance of the AMS in multilayer systems in fold and thrust belts. Example from the Eocene turbidites from Southern Pyrenees. *Geological Journal,* **45** (5-6), 544-561.

Ritcher, C. & Van der Pluijm, B. A. 1994. Separation of paramagnetic and ferrimagnetic susceptibilities using low temperature magnetic susceptibilities and comparison with high field methods. *Physics of the Earth and Planetary Interiors,* **82**, 113-123.

Sarkarinejad, K. & Azizi, A. 2008. Slip partitioning and inclined dextral transpression along the Zagros Thrust System, Iran. *Journal of Structural Geology*, **30**(1), 116-136.

Sarkarinejad, K., Faghih, A. & Grasemann, B. 2008. Transpressional deformations within the Sanandaj–Sirjan metamorphic belt (Zagros Mountains, Iran). *Journal of Structural Geology*, ***30***(7), 818-826.

Scheck-Wenderoth, M. & Lamarche, J. 2005. Crustal memory and basin evolution in the Central European Basin System—new insights from a 3D structural model. *Tectonophysics*, **397**(1), 143-165.

Scheck, M., Bayer, U., Otto, V., Lamarche, J., Banka, D. & Pharaoh, T. 2002. The Elbe Fault System in North Central Europe—a basement controlled zone of crustal weakness. *Tectonophysics*, **360**(1), 281-299.

Schleicher, A. M., van der Pluijm B. A. & Warr, L. N. 2012. Chlorite-smectite clay minerals and fault behavior: new evidence from the San Andreas Fault Observatory at Depth (SAFOD) core. *Lithosphere*, **4**(3), 209-220.

Schito, A., Corrado, S., Trolese, M., Aldega, L., Caricchi, C., Cirilli, S., Grigo, D., Guedes, A., Romano, C., Spina, A. & Valentim, B. 2017. Assessment of thermal evolution of Paleozoic successions of the Holy Cross Mountains (Poland). *Marine and Petroleum Geology*, **80**, 112-132.

Simón-Gómez, J. L. 1989. Late Cenozoic stress field and fracturing in the Iberian Chain and Ebro Basin (Spain). *Journal of Structural Geology*, **11**(3), 285-294.

Simón, J. L. & Liesa, C. L. 2011. Incremental slip history of a thrust: diverse transport directions and internal folding of the Utrillas thrust sheet (NE Iberian Chain, Sapin). *Geological Society, London, Special Publications,* **349**, 77-97.

Simón, J. L. & Paricio, J. 1988. Sobre la compresión neógena en la Cordillera Ibérica. *Estudios Geológicos*, **44**, 271–283.

Smeraglia, L., Aldega, L., Billi, A., Carminati, E. & Doglioni, C. 2016. Phyllosilicate injection along extensional carbonate-hosted faults and implications for co-seismic slip propagation: Case studies from the central Apennines, Italy. *Journal of Structural Geology*, **93**, 29-50.

Solum, J. G. & van der Pluijm, B. A. 2009. Quantification of fabrics in clay gouge from the Carboneras fault, Spain and implications for fault behavior. *Tectonophysics*, **475**(3), 554-562.

Środoń, J. 1999. Nature of mixed layer clays and mechanisms of their formation and alteration. *Annual Review of Earth and Planetary Sciences*, **27**, 19–53.

Toy, V. G., Prior, D. J. & Norris, R. J. 2008. Quartz fabrics in the Alpine Fault mylonites: Influence of pre-existing preferred orientations on fabric development during progressive uplift. *Journal of Structural Geology*, **30**, 602-621.

Van Hinsbergen, D. J. J., Cunningham, D., Straathof, G. B., Ganerod, M., Hendriks, B. W. H. & Dijkstra, A. H. 2015. Triassic to Cenozoic multi-stage intra-plate deformation focused near the Bogd Fault system, Gobi Altai, Mongolia. *Geoscience Frontiers*, **6**, 723-740.

Villena, J., Pérez, A., Pardo, G. & González, A. 1991. Sedimentología del Terciario. In: Mapa Geológico de Daroca 1:200.000. *Instituto Tecnológico GeoMinero de España*, **40** (7-5), 138-174.

Vrolijkm P. & van der Pluijm B.A. 1999. Clay gouge. *Journal of Structural Geology*, **21**(8), 1039–1048.

Woodcock, N.H. & Rickards, B. 2003. Transpressive duplex and flower structure: Dent Fault system, NW England. *Journal of Structural Geology*, **25**, 1981-1992.

Ziegler, P. A. 1989. Geodynamic model for Alpine intraplate compressional deformation in Western and Central Europe. In: Cooper, M. A., and Williams, G. D. (Eds.), Inversion Tectonics. *Geological Society Special Publication,* **44**, 63-85.

Table captions

Table 1. Location of sites and type of measured data (European Datum ED50 for geographic coordinates). D. T. D. NRM: Thermal demagnetization of the Natural Remnant Magnetization.

Table 2. X-ray diffraction mineralogical assemblages of fault rocks. Acronyms: Qtz = quartz; Cal = calcite; Dol = dolomite; Phy = phyllosilicates; Gy = Gypsum; Hem = Hematite; Go= goethite; Kln = kaolinite; Chl = chlorite; I-S = mixed layer illite-smectite; I = illite; R = stacking order; %I in I-S = illite content in mixed layer illite-smectite; tr stands for traces (<1%); HW = hanging-wall; FW= footwall.

Table 3. Site-mean AMS parameters. N: number of specimens analysed at each site; Km: magnitude of the magnetic susceptibility (in 10^{-6} SI); P': corrected anisotropy degree; T: shape parameter; St. dev.: standard deviation.

Table 4. Site-mean AMS directional data. k_{max}, k_{int}, k_{min}: orientation of mean principal susceptibility axes (T/P: trend/plunge) considering Jelinek statistics (Jelinek, 1978); Conf. angles: confidence angles.

Table 5. Site-mean AMS directional and scalar data for sites analysed at room and low temperatures. N: number of analysed samples; k_{max}, k_{int}, k_{min}: orientation of principal axes (T/P: trend/plunge) considering Jelinek statistics; Conf. ang.: confidence angles; Km: magnitude of the magnetic susceptibility (in 10^{-6} SI); Km-LT/Km-RT: ratio between magnetic susceptibility at low temperature and at room temperature; P': corrected anisotropy degree; T: shape parameter.

Figure captions

Figure 1. A) Location of the studied zone within the eastern part of the Iberian Plate. B) The Daroca thrust within the Iberian Chain (Aragonian Branch).

Figure 2. A) Geological map of the Daroca thrust with the location of studied sites and stereoplot (equal area projection, lower hemisphere) of some related-reverse surfaces. B) Cross section of the Daroca thrust (marked in Fig. 2A). C) Panoramic view of the northwestern part of the Daroca thrust. D) Close-up view of the frontal footwall flat of the thrust. E, F) Photograph and geological sketch showing the southernmost part of the Daroca thrust (sites 1 to 10) where the maximum thickness of the fault breccia and gouge is preserved.

Figure 3. Photographs, structural data and litho-structural transects of several sites of the northwestern part of the Daroca thrust. Stereoplots have been made with R. W. Allmendinger´s Stereonet program (Allmendinger *et al.*, 2013; Cardozo and Allmendinger, 2013). A) Close-up photographs, structural data and litho-structural transects in sites 14, 15 and 16. Notice the S-C structures and the sigmoidal bodies developed from the brecciated hanging-wall Cambrian dolostones. In site 14, the footwall Aragonian conglomerates exhibit a scarce brecciated texture. B, C) Photograph (marked in Fig. 2D) and geological sketch of the frontal area of the Daroca thrust. The location of two litho-structural transects is shown. D) Structural data in the Cambrian dolostones in site 11. E) Close-up photographs, structural data and litho-structural transect of site 12.

Figure 4. Photographs, structural data and litho-structural transect from the southerneast part of the Daroca thrust. The location of different studied sites along the synthetic transect are indicated. Stereoplots

have been made with R. W. Allmendinger´s Stereonet program (Allmendinger *et al.*, 2013; Cardozo and Allmendinger 2013). Symbols for stereoplots and legend of the litho-structural transects as in Fig. 3.

Figure 5. A) Geological sketch of site 7 showing the main extensional structures affecting the hanging-wall Aragonian conglomerates. B) Synthetic stereoplot (equal area projection, lower hemisphere) of extensional faults of the Aragonian materials throughout the study area.

Figure 6. A) Equal area projection of AMS directional data for the total of measured samples (lower hemisphere projection, mean vectors and confidence ellipses considering Jelinek statistics). B) Corrected anisotropy degree (P') *versus* bulk magnetic susceptibility (Km) for the total measured samples. C) Shape parameter (T) *versus* the corrected anisotropy degree (P') for the total measured samples.

Figure 7. A) Temperature dependent magnetic susceptibility (*k*-T) curves for samples from sites 1, 8, 9 and 16 (samples HD1, HD9-12, HD6-6 and HD10-3). In red: heating curve, in blue: cooling curve, in green: hyperbolic adjustment to paramagnetic behaviour (Hrouda *et al.*, 1997). B) Thermal demagnetization of the NRM for samples from sites 1, 8 and 9 (samples HD1-8, HD9-2 and HD6-4).

Figure 8. Equal area projection of AMS directional data and mean of structural data for each measured site (lower hemisphere projection, mean vectors and confidence ellipses considering Jelinek statistics).

Figure 9. A) Equal area projection of AMS directional data at room temperature (black symbols) and AMS directional data at low temperature (grey symbols). Lower hemisphere projection, mean vectors and confidence ellipses considering Jelinek statistics. B) Diagrams of magnetic susceptibility at room temperature (Km-RT) versus magnetic susceptibility at low temperature (Km-LT).

Figure 10. Comparison between tectonic and magnetic fabrics in an intensively analysed hand specimen (HD2, site 2). (A) Section of the specimen; S: main foliation; ESB: extensional shear band. (B) Detail view of tectonic fabric in thin section; cf: cataclastic fragment. (C) Stereoplot of structural elements: S and C planes, and extensional shear band (ESB). (D) Stereoplot of AMS axes (mean vectors considering Jelinek statistic).

Figure 11. Synthetic stereoplots considering the whole mesostructural and AMS datasets: A) mean AMS tensor (k_{maxM}, k_{intM} and k_{minM}) obtained from the whole of 189 analysed specimens (Jelinek statistics, Jelinek, 1978); B) mean AMS tensor (local tensor, k_{maxL}, k_{intL} and k_{minL}) obtained from the six AMS site means (Fisher statistics, Fisher, 1953); C) mean Fisher vector of poles to S and C planes, obtained from the site means (Fisher statistics, Fisher, 1953), and inferred transport directions; D) superposition of k_{minM} and $k_{minL,}$ and the means of poles to S and C planes; E) superposition of k_{max} site means, the inferred transport directions, and k_{maxM} and k_{maxL}.

Figure 12. Sketches showing interpretative models for the macrostructure of the Daroca thrust considering: A) Reactivation of Variscan flexural-slip folds. B) Tightening of a previous fault-bend fold. C) Positive flower structure associated with strike-slip faulting.

Table 1. *Sites*

Sector	Site	Latitude	Longitude	Structural data	Thin section	X-ray	AMS	k-T curves	T. D. NRM
SOUTHERN	1	N41°6'35.5"	W1°24'28.1"			X (5 samples)	X	X	X
	2	N41°6'35.4"	W1°24'28.1"	X	X (2)		X	X	X
	3	N41°6'35.1"	W1°24'28.1"	X		X	X	X	X
	4	N41°6'35.3"	W1°24'28.5"	X					
	5	N41°6'36.6	N1°24'28.0"		X				
	6	N41°6'34.0"	W1°24'28.5"	X					
	7	N41°6'32.0"	W1°24'29.4"	X					
	8	N41°6'37.8"	W1°24'28.9"				X	X	X
	9	N41°6'39.1"	W1°24'31.0"	X	X	X	X	X	X
	10	N41°6'39.0"	W1°24'32.0"	X					
NORTHERN	11	N41°7'5.3"	W1°24'52.8"	X					
	12	N41°7'3.5"	W1°24'52.0"	X					
	13	N41°7'43.8"	W1°24'47.3"		X	X			
	14	N41°7'0.3"	W1°24'37.0"	X					
	15	N41°7'0.3"	W1°24'37.0"	X					
	16	N41°7'0.3"	W1°24'37.0"	X			X	X	X

Table 1. Location of sites and type of measured data (European Datum ED50 for geographic coordinates). T. D. NRM: Thermal demagnetization of the Natural Remnant Magnetization.

Table 2. *X-ray diffraction mineralogical assemblages of fault rocks*

Site	Sample	Rock Type	whole-rock composition (%wt.)							<2µm grain-size fraction (%wt.)				R	%I in I-S
			Qtz	Cal	Dol	Phy	Gy	Hem	Go	I	I-S	Kln	Chl		
1	HD1a	foliated lutite (HW)	10	-	6	82	-	2	-	73	8	-	19	0	10
3	HD3c	cataclasite (HW)	15	5	-	78	2	-	-	57	7	-	36	0	10
9	HD6a	foliated lutite (HW)	15	10	tr	75	-	-	-	70	7	12	11	0	10
1	HD1b	gouge (FW)	9	25	1	65	-	-	tr	51	11	-	38	0	15
1	HD1c	cataclasite (FW)	19	-	-	78	-	3	tr	58	7	30	5	0	10
1	HD1d	gouge (FW)	12	3	1	84	-	tr	tr	55	12	5	28	0	15
1	HD1f	gouge (FW)	17	-	-	82	-	1	-	56	15	10	18	0	20
13	HD11a	microbreccia (FW)	18	2	5	75	-	-	-	58	12	19	11	0	10

Table 2. X-ray diffraction mineralogical assemblages of fault rocks. Acronyms: Qtz = quartz; Cal = calcite; Dol = dolomite; Phy = phyllosilicates; Gy = Gypsum; Hem = Hematite; Go= goethite; Kln = kaolinite; Chl = chlorite; I-S = mixed layer illite-smectite; I = illite; R = stacking order; %I in I-S = illite content in mixed layer illite-smectite; tr stands for traces (<1%); HW = hanging-wall; FW= footwall.

Table 3. *Site-mean AMS parameters*

Site	N	Unit	Km ($\times 10^{-6}$ SI)	St. dev. ($\times 10^{-6}$ SI)	P'	St. dev.	T	St. dev.
1	12	Fault gouge (bottom)	275	38	1.042	0.012	0.240	0.526
2	68	Fault gouge (bottom)	215	30	1.079	0.027	0.060	0.280
3	11	Fault gouge (bottom)	221	33	1.054	0.020	0.345	0.246
8	12	Fault gouge (middle)	282	54	1.065	0.013	0.322	0.236
9	74	Fault gouge (roof)	217	40	1.041	0.022	0.250	0.374
16	12	Fault microbreccia	238	31	1.031	0.010	-0.109	0.432

Table 3. *Site-mean AMS parameters.* N: number of specimens analysed at each site; Km: magnitude of the magnetic susceptibility (in 10^{-6} SI); P': corrected anisotropy degree; T: shape parameter; St. dev.: standard deviation.

Table 4. *Site-mean AMS directional data*

Site	k_{max} (T/P)(º)	Conf. angles (º)	k_{int} (T/P) (º)	Conf. angles (º)	k_{min} (T/P) (º)	Conf. angles (º)	Structural data (Strike/Dip) (º)
1	262/23	32/15	360/17	32/28	123/61	28/13	130,15S; thrust plane
2	284/23	29/10	173/40	29/16	035/41	17/10	132,43S; S plane
							119,21S; C plane
3	343/5	23/15	074/12	21/17	230/77	23/16	158,54W; S plane
							161,31W; C plane
8	150/4	14/10	246/52	14/9	57/37	10/9	120,20S; S plane
9	129/14	35/23	220/5	43/33	329/75	42/24	155,58W; S plane
							128,33S; C plane
16	325/17	15/7	056/3	16/11	155/72	13/7	175,43W; S plane
							032,5W; thrust plane

Table 4. Site-mean AMS directional data. k_{max}, k_{int}, k_{min}: orientation of mean principal susceptibility axes (T/P: trend/plunge) considering Jelinek statistics (Jelinek, 1978); Conf. angles: confidence angles.

Table 5. *Site-mean AMS directional and scalar data for sites analyzed at room and low temperatures*

Site	N	K_{max} (T/P) (º)	Conf. ang. (º)	K_{int} (T/P) (º)	Conf. ang. (º)	K_{min} (T/P) (º)	Conf. ang. (º)	Km 10^{-6} SI	Km-LT/ Km-RT	P'	T
8-RT	6	149/08	17/10	249/48	17/6	053/40	11/6	290	1.90	1.073	0.355
8-LT	*6*	*149/08*	*15/9*	*250/51*	*14/6*	*053/38*	*11/5*	*551*		*1.024*	*0.268*
16-RT	6	317/19	15/9	050/8	16/10	163/69	14/8	255	3.01	1.030	-0.051
16-LT	*6*	*316/22*	*13/9*	*049/8*	*13/12*	*158/67*	*14/9*	*768*		*1.047*	*-0.107*

Table 5. Site-mean AMS directional and scalar data for sites analysed at room and low temperatures. N: number of analysed samples; k_{max}, k_{int}, k_{min}: orientation of principal susceptibility axes (T/P: trend/plunge) considering Jelinek statistics; Conf. ang.: confidence angles; Km: magnitude of the magnetic susceptibility (in 10^{-6} SI); Km-LT/Km-RT: ratio between magnetic susceptibility at low temperature and at room temperature; P': corrected anisotropy degree; T: shape parameter.

Highlights

- AMS applied to study of faults rocks at shallow crustal levels
- Magnetic ellipsoids axes compared to kinematic indicators on faults
- Contribution to fault kinematics and driving mechanisms of intraplate deformation
- Contribution to Cenozoic intraplate deformation in North Iberia

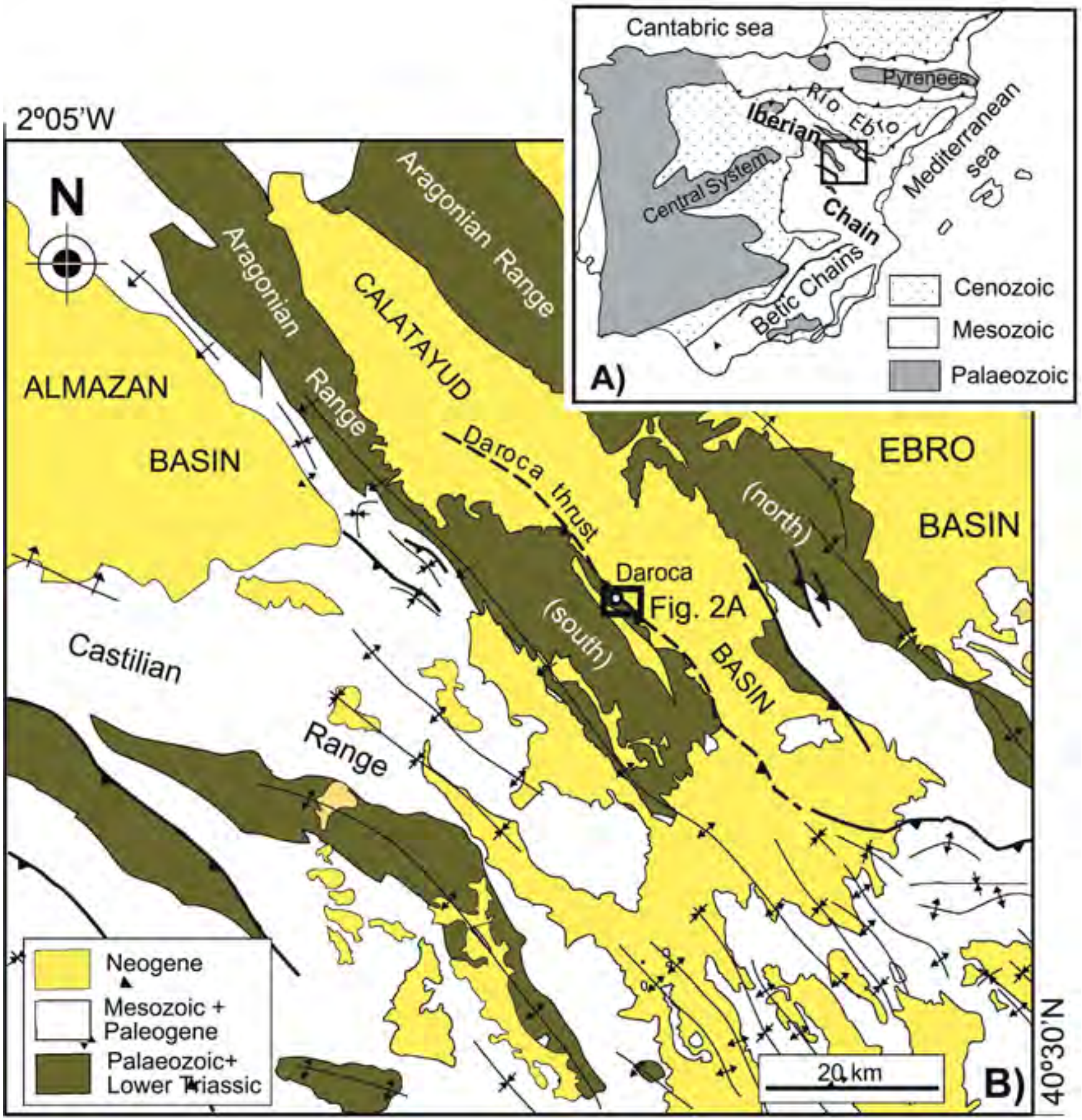
Cantabric sea
Pyrenees
Río Ebro
Iberian
Chain
Central System
Mediterranean sea
Betic Chains
Cenozoic
Mesozoic
Palaeozoic
A)
2°05'W
N
Aragonian Range
Aragonian Range
CALATAYUD
ALMAZAN
BASIN
Daroca thrust
EBRO
BASIN
(north)
Daroca
Fig. 2A
(south)
BASIN
Castilian
Range
Neogene
Mesozoic + Paleogene
Palaeozoic+ Lower Triassic
20 km
B)
40°30'N

Figure 1

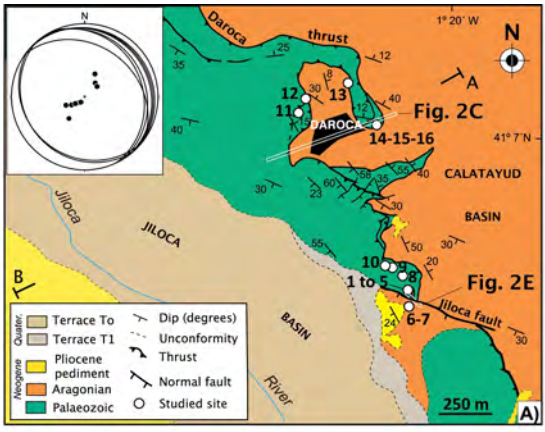
N
Daroca
thrust
1° 20' W
N
A
Fig. 2C
DAROCA
14-15-16
41° 7' N
CALATAYUD
BASIN
Jiloca
JILOCA
B
Fig. 2E
1 to 5
6-7
Jiloca fault
BASIN
River
250 m
A)
Terrace To
Terrace T1
Pliocene pediment
Aragonian
Palaeozoic
Dip (degrees)
Unconformity
Thrust
Normal fault
Studied site
Quater.
Neogene

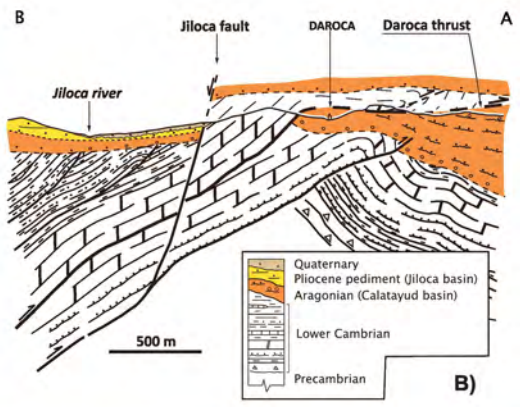
B
Jiloca fault
DAROCA
Daroca thrust
A
Jiloca river
500 m
Quaternary
Pliocene pediment (Jiloca basin)
Aragonian (Calatayud basin)
Lower Cambrian
Precambrian
B)


SW
NE
Hanging-wall Cambrian dolostones
Footwall Aragonian conglomerates
Footwall Aragonian conglomerates
C)


Hanging-wall Cambrian dolostones
Footwall Aragonian conglomerates
Fig. 3B
D)


E)

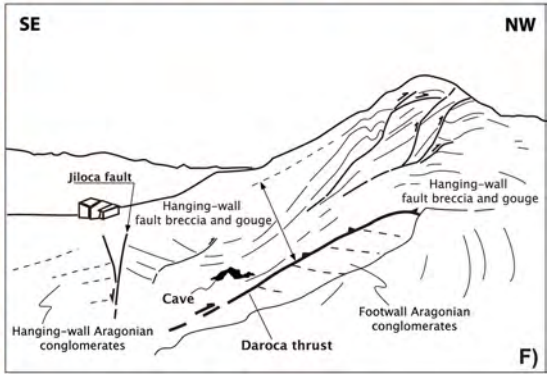
SE
NW
Jiloca fault
Hanging-wall fault breccia and gouge
Hanging-wall fault breccia and gouge
Cave
Hanging-wall Aragonian conglomerates
Daroca thrust
Footwall Aragonian conglomerates
F)

Figure 2

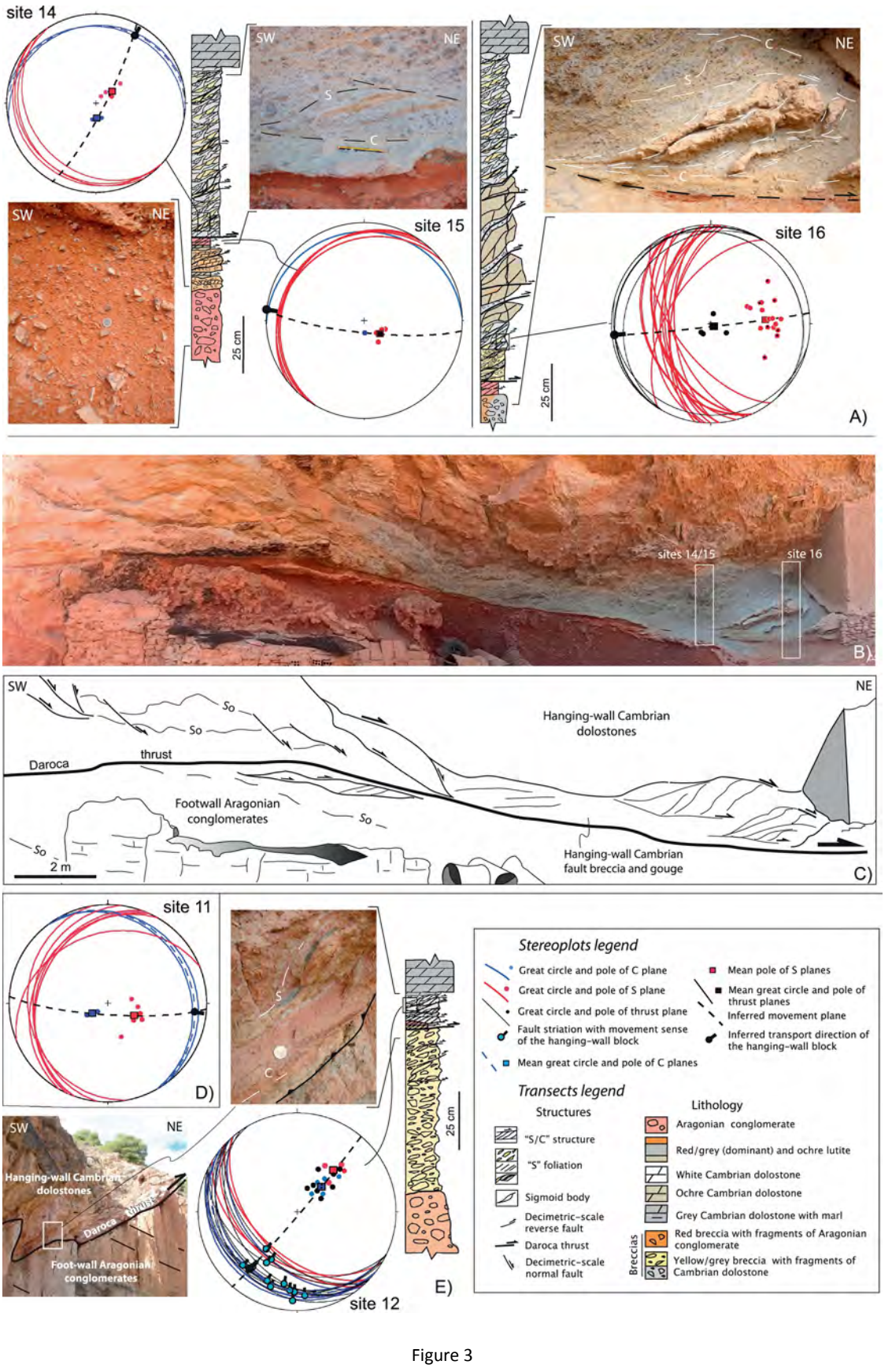
site 14
SW
NE
S
C
site 15
25 cm
site 16
A)
sites 14/15
site 16
B)
So
Hanging-wall Cambrian dolostones
Daroca thrust
Footwall Aragonian conglomerates
2 m
Hanging-wall Cambrian fault breccia and gouge
C)
site 11
D)
site 12
E)
Hanging-wall Cambrian dolostones
Daroca thrust
Foot-wall Aragonian conglomerates
Stereoplots legend
Great circle and pole of C plane
Great circle and pole of S plane
Great circle and pole of thrust plane
Fault striation with movement sense of the hanging-wall block
Mean great circle and pole of C planes
Mean pole of S planes
Mean great circle and pole of thrust planes
Inferred movement plane
Inferred transport direction of the hanging-wall block
Transects legend
Structures
"S/C" structure
"S" foliation
Sigmoid body
Decimetric-scale reverse fault
Daroca thrust
Decimetric-scale normal fault
Lithology
Aragonian conglomerate
Red/grey (dominant) and ochre lutite
White Cambrian dolostone
Ochre Cambrian dolostone
Grey Cambrian dolostone with marl
Breccias
Red breccia with fragments of Aragonian conglomerate
Yellow/grey breccia with fragments of Cambrian dolostone

Figure 3

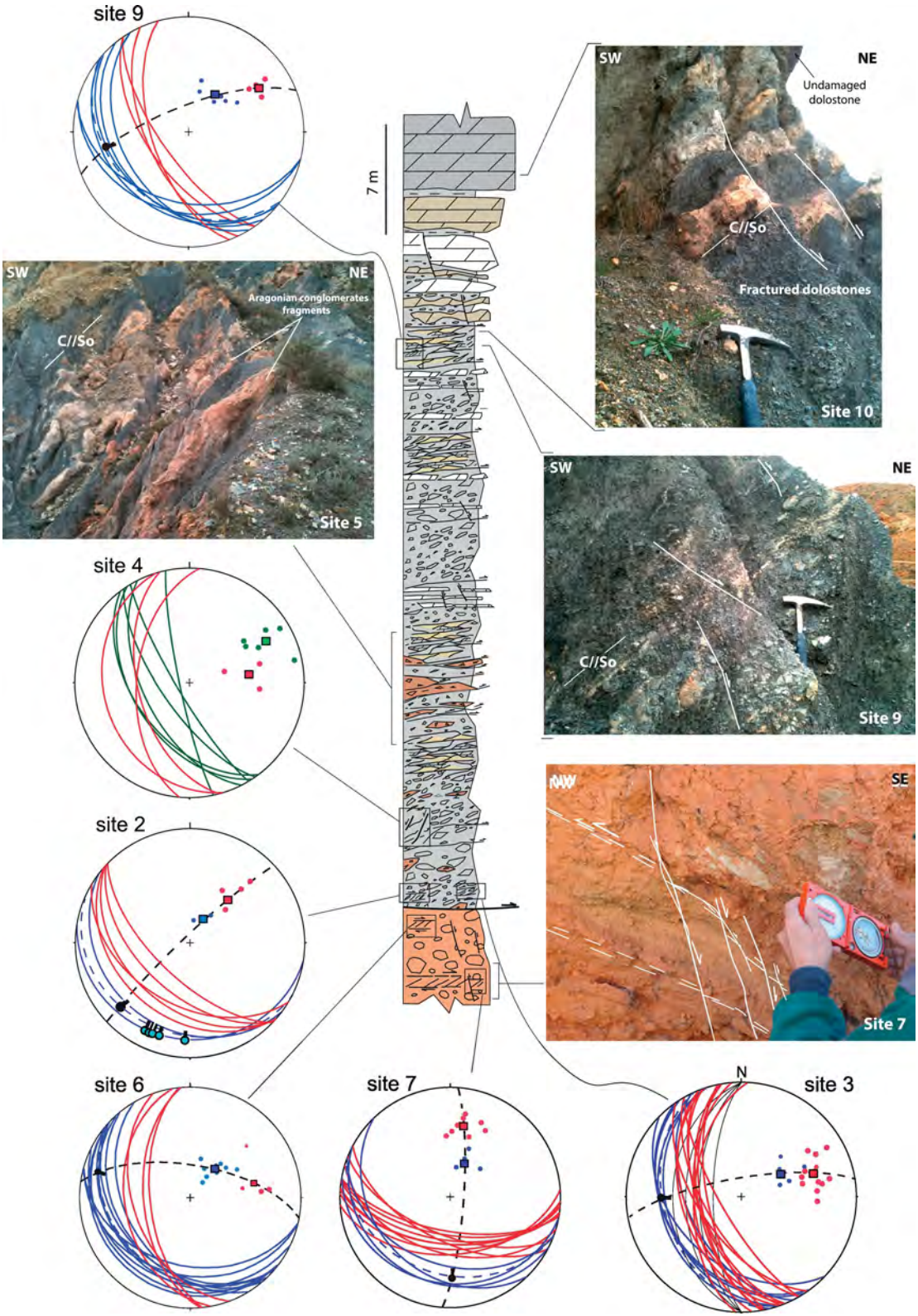
site 9
7 m
SW
NE
Undamaged dolostone
C//So
Fractured dolostones
Site 10
SW
NE
Aragonian conglomerates fragments
C//So
Site 5
SW
NE
C//So
Site 9
site 4
site 2
NW
SE
Site 7
site 6
site 7
N
site 3

Figure 4

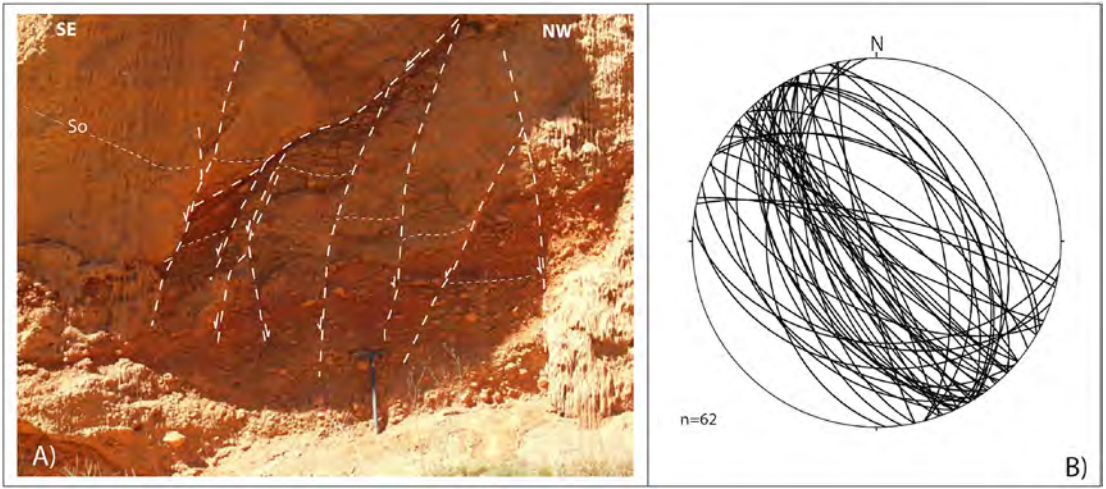

Figure 5

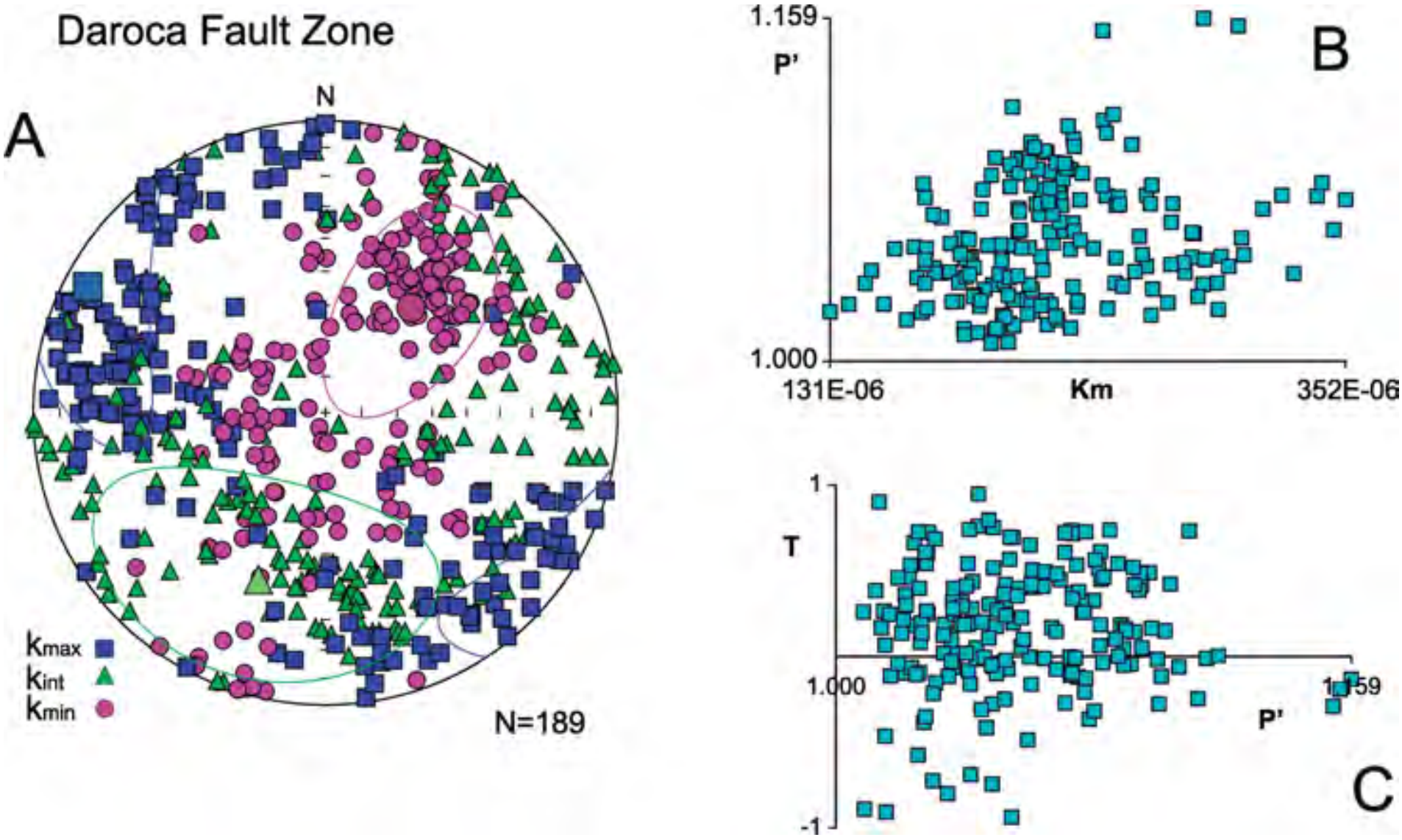
Daroca Fault Zone
A
N
kmax
kint
kmin
N=189
1.159
P'
1.000
131E-06
Km
352E-06
B
1
T
1.000
P'
-1
C

Figure 6

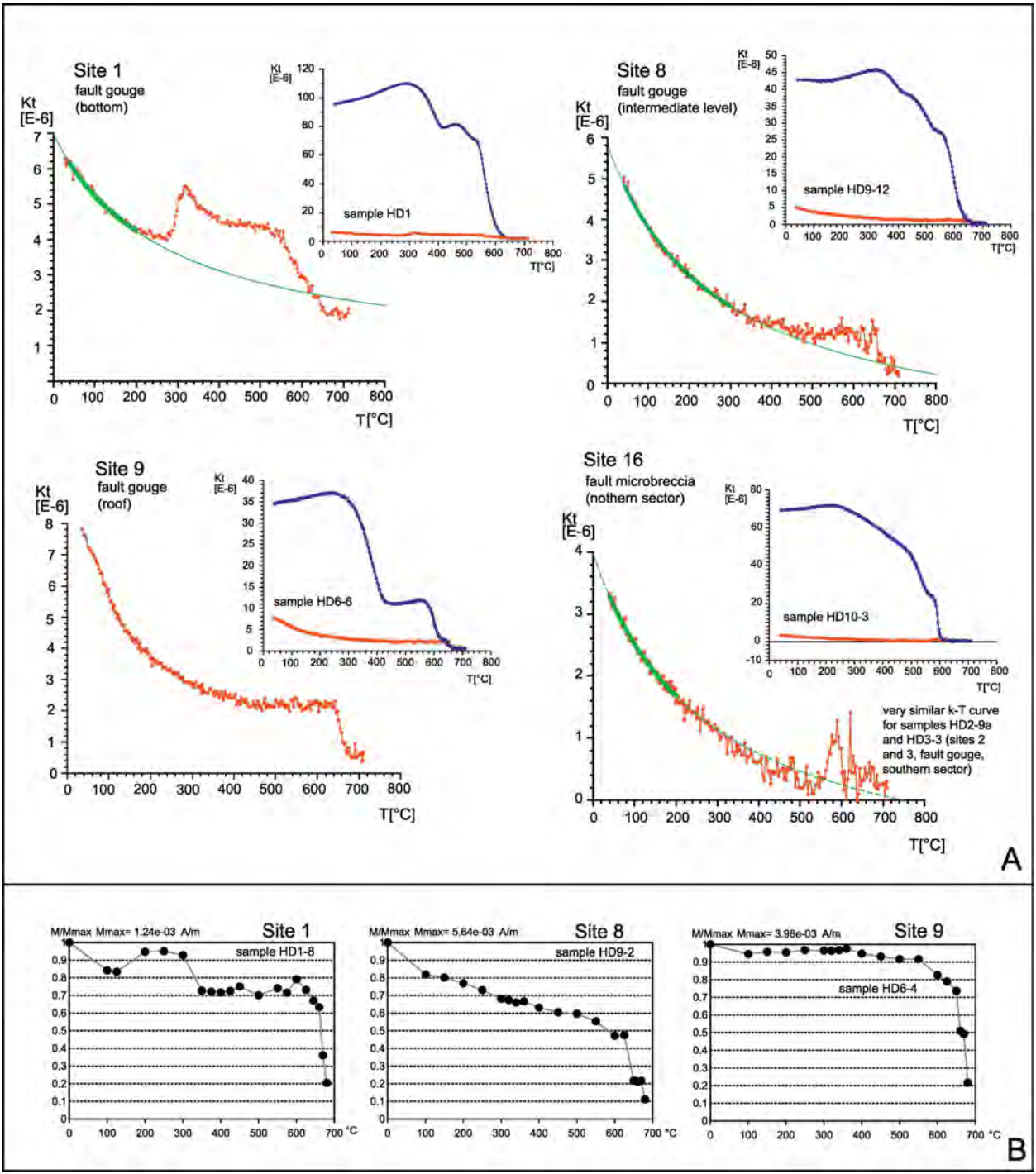
Site 1
fault gouge
(bottom)
Kt
[E-6]
T[°C]
sample HD1
Site 8
fault gouge
(intermediate level)
sample HD9-12
Site 9
fault gouge
(roof)
sample HD6-6
Site 16
fault microbreccia
(nothern sector)
sample HD10-3
very similar k-T curve
for samples HD2-9a
and HD3-3 (sites 2
and 3, fault gouge,
southern sector)
A
M/Mmax Mmax= 1.24e-03 A/m
Site 1
sample HD1-8
M/Mmax Mmax= 5.64e-03 A/m
Site 8
sample HD9-2
M/Mmax Mmax= 3.98e-03 A/m
Site 9
sample HD6-4
°C
B

Figure 7

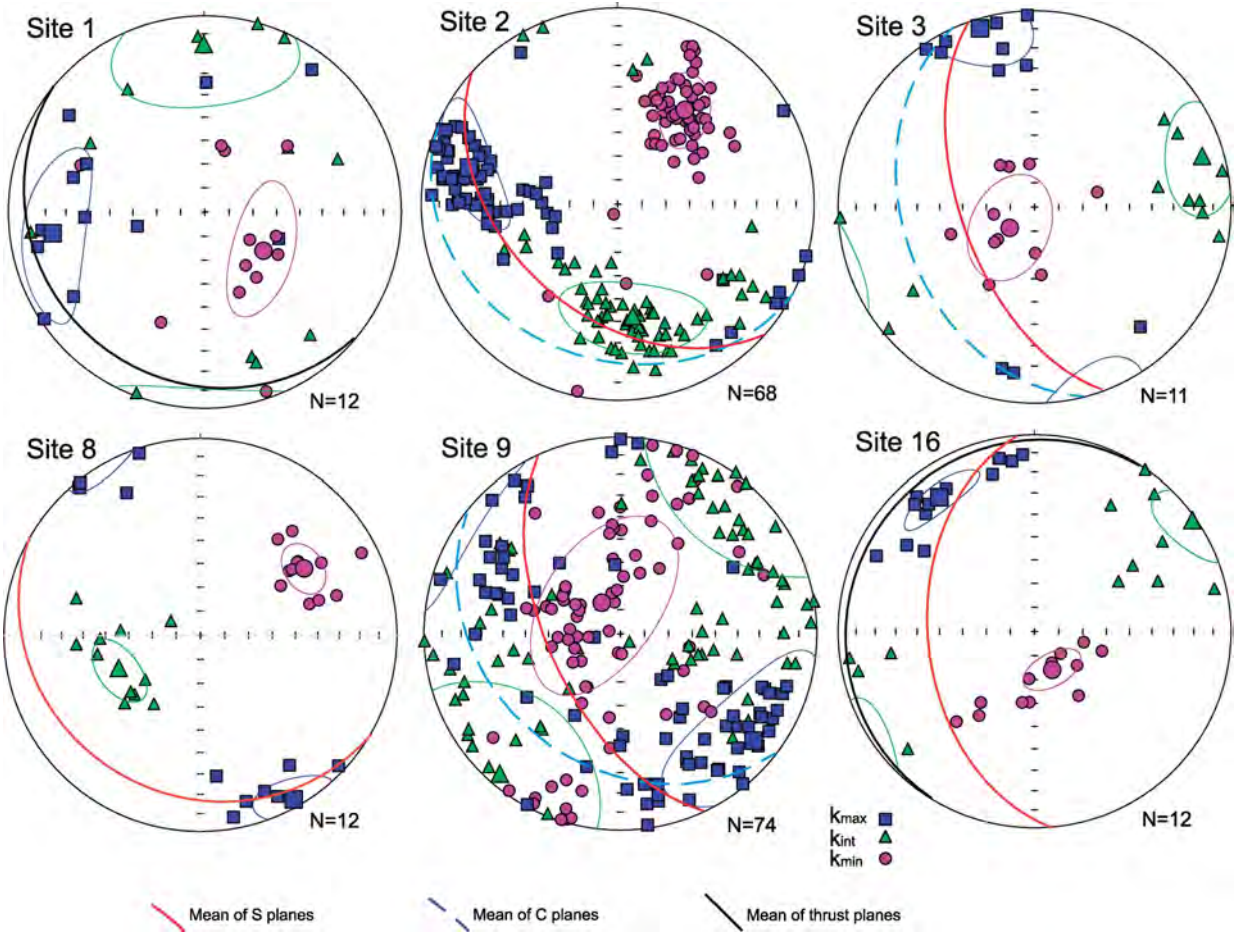
Site 1
N=12
Site 2
N=68
Site 3
N=11
Site 8
N=12
Site 9
N=74
Site 16
N=12
kmax
kint
kmin
Mean of S planes
Mean of C planes
Mean of thrust planes

Figure 8

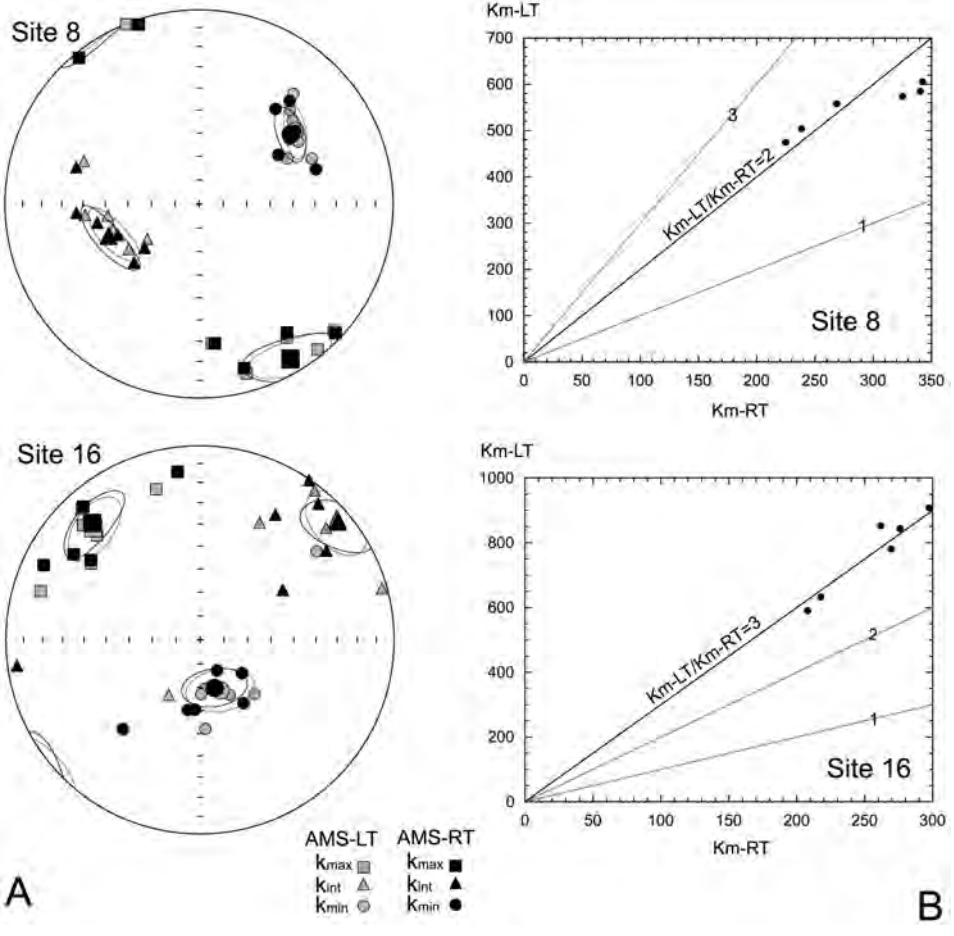
Site 8
Km-LT
Km-RT
Km-LT/Km-RT=2
3
1
Site 8
Site 16
Km-LT/Km-RT=3
2
1
Site 16
AMS-LT
AMS-RT
Kmax
Kint
Kmin
A
B

Figure 9

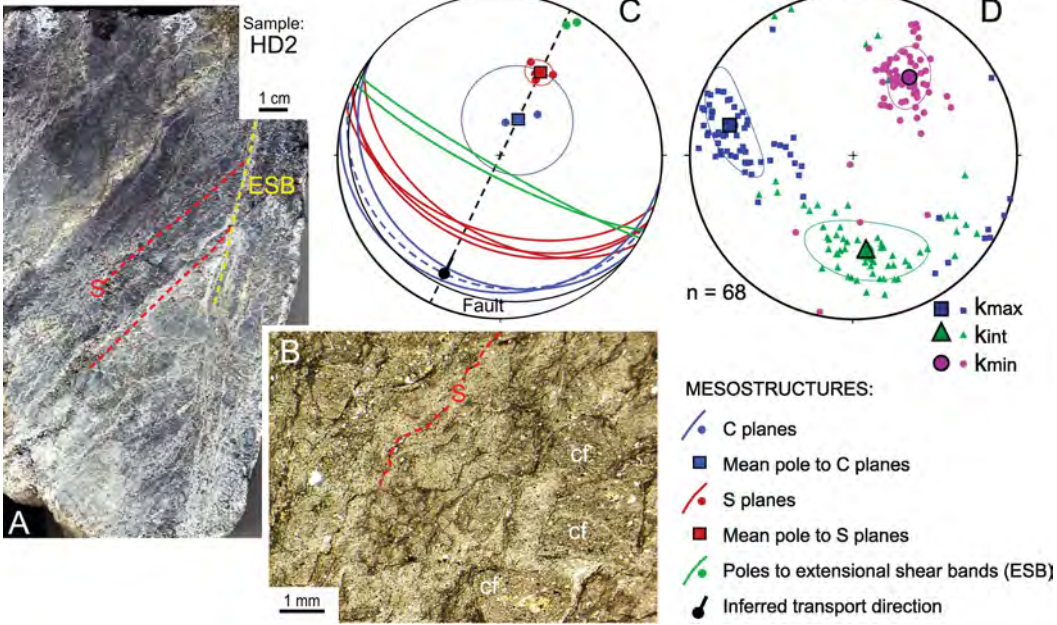
Sample:
HD2
1 cm
ESB
S
A
B
S
cf
cf
cf
1 mm
C
Fault
D
n = 68
kmax
kint
kmin
MESOSTRUCTURES:
C planes
Mean pole to C planes
S planes
Mean pole to S planes
Poles to extensional shear bands (ESB)
Inferred transport direction

Figure 10

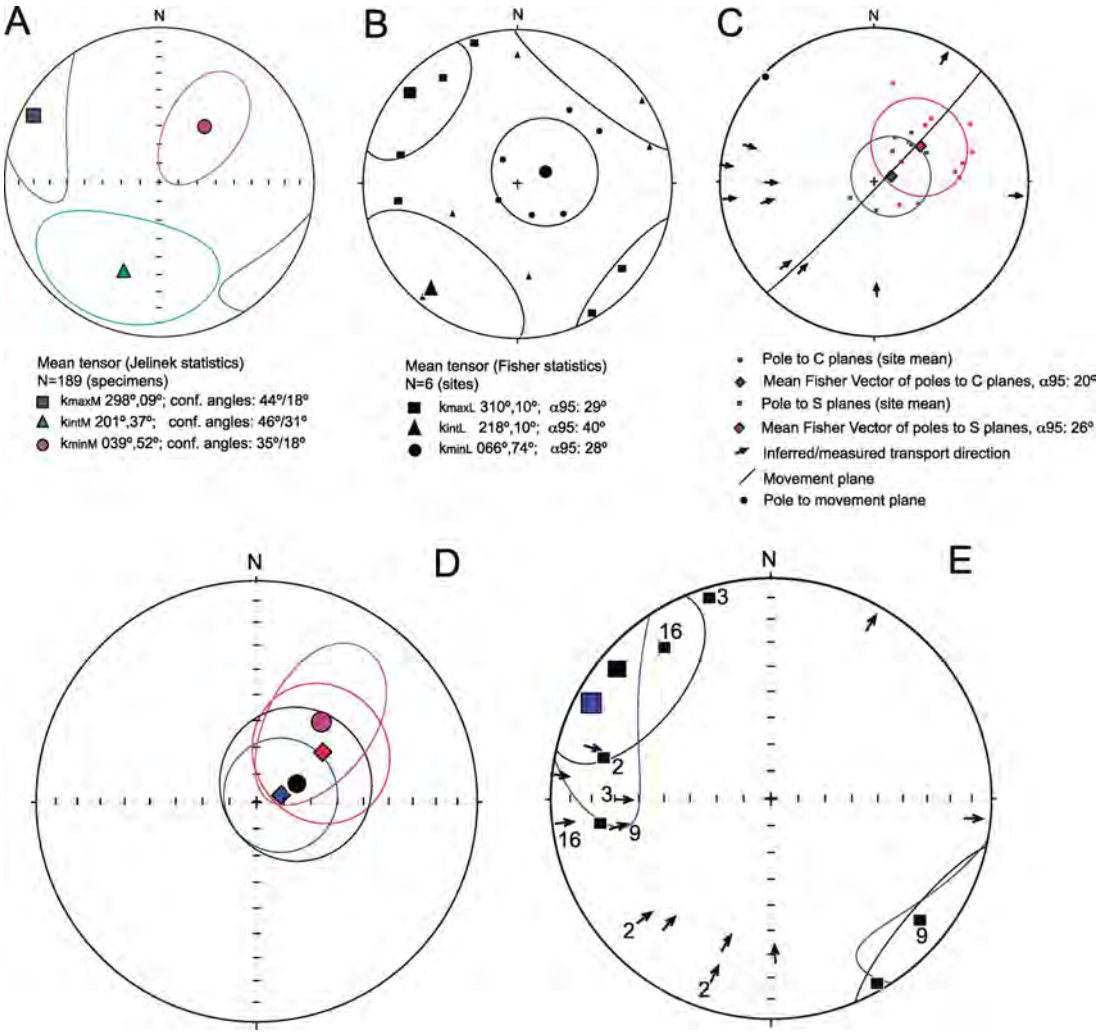
A
N
Mean tensor (Jelinek statistics)
N=189 (specimens)
kmaxM 298°,09°; conf. angles: 44°/18°
kintM 201°,37°; conf. angles: 46°/31°
kminM 039°,52°; conf. angles: 35°/18°
B
N
Mean tensor (Fisher statistics)
N=6 (sites)
kmaxL 310°,10°; α95: 29°
kintL 218°,10°; α95: 40°
kminL 066°,74°; α95: 28°
C
N
Pole to C planes (site mean)
Mean Fisher Vector of poles to C planes, α95: 20°
Pole to S planes (site mean)
Mean Fisher Vector of poles to S planes, α95: 26°
Inferred/measured transport direction
Movement plane
Pole to movement plane
D
N
E
N
3
16
2
3
16
9
2
2
9

Figure 11

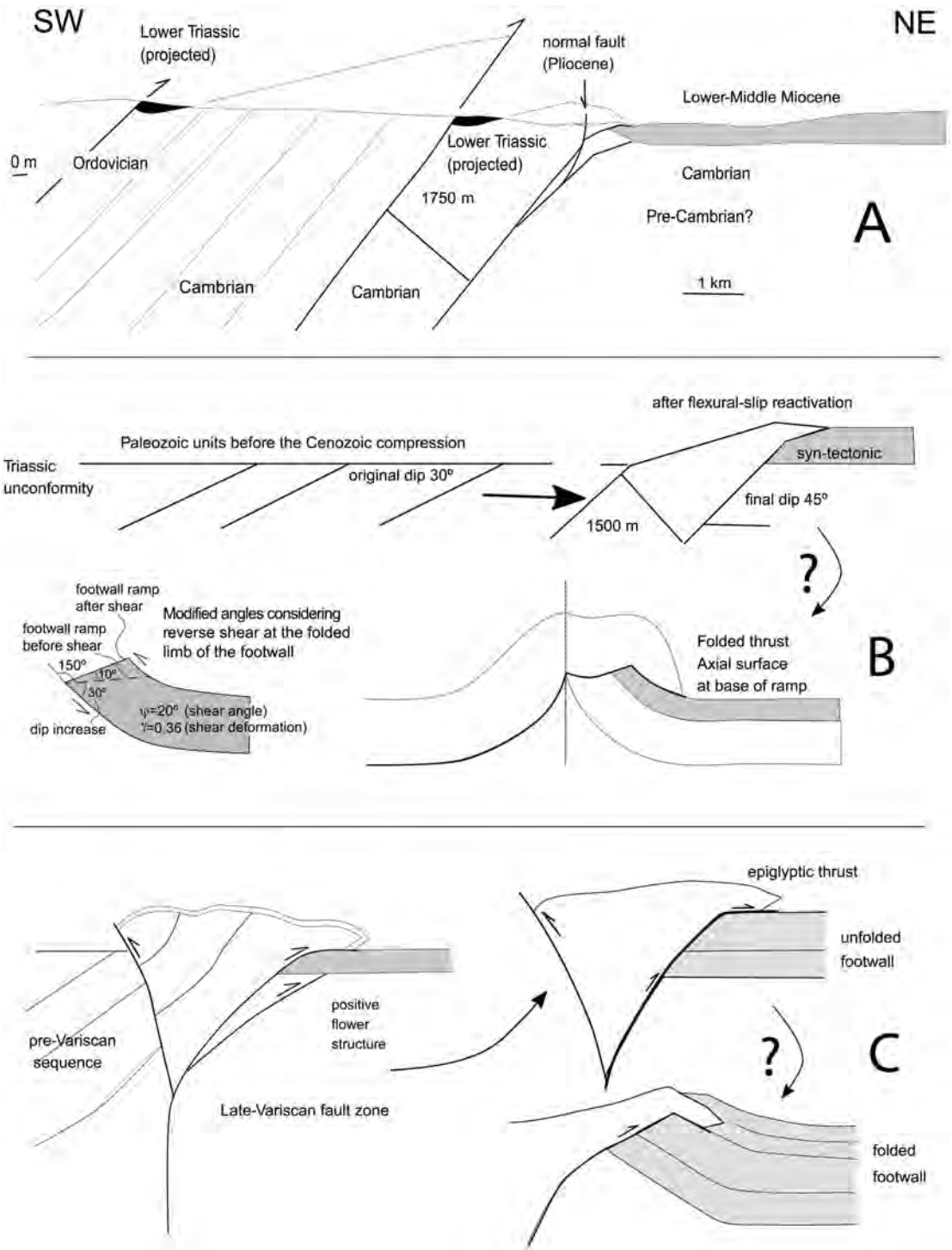
SW
NE
Lower Triassic
(projected)
normal fault
(Pliocene)
Lower-Middle Miocene
0 m
Ordovician
Lower Triassic
(projected)
Cambrian
1750 m
Pre-Cambrian?
A
Cambrian
Cambrian
1 km
after flexural-slip reactivation
Paleozoic units before the Cenozoic compression
Triassic
unconformity
original dip 30º
syn-tectonic
final dip 45º
1500 m
?
footwall ramp
after shear
footwall ramp
before shear
Modified angles considering
reverse shear at the folded
limb of the footwall
150º
120º
30º
ψ=20º (shear angle)
γ=0.36 (shear deformation)
dip increase
Folded thrust
Axial surface
at base of ramp
B
epiglyptic thrust
unfolded
footwall
positive
flower
structure
pre-Variscan
sequence
?
C
Late-Variscan fault zone
folded
footwall

Figure 12